Matter

CellPress

Article

Single-Molecule Toroic Design through Magnetic Exchange Coupling

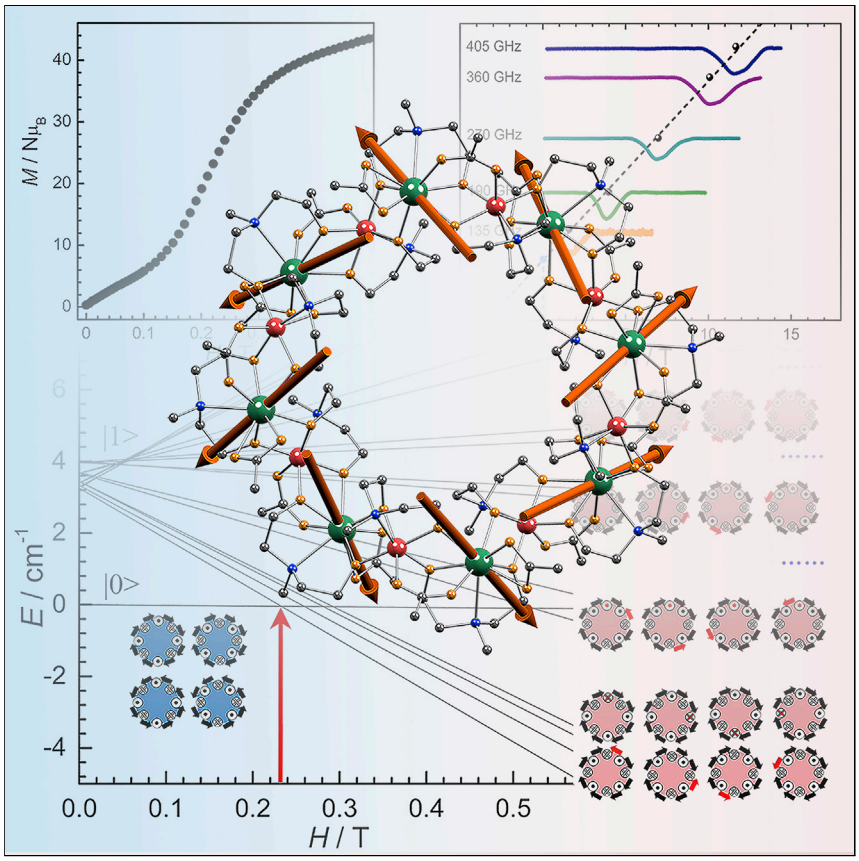

A circular molecule named $\{Fe_8Dy_8\}$ with fixed toroidal magnetic moment below a certain temperature can be used for high-density information storage. The energy gap between this toroidal ground state (blue molecule) and the first excited state (reddish molecule) causes the S-shaped magnetization plot at low field, while such a toroidal moment is caused by the ferromagnetic exchange interaction between the metal centers. The strong magnetic anisotropy of the dysprosium(III) ions determines the toroidal directions (arrows in the molecular wheel).

Hao-Lan Zhang, Yuan-Qi Zhai, Lei Qin, Liviu Ungur, Hiroyuki Nojiri, Yan-Zhen Zheng

zheng.yanzhen@xjtu.edu.cn

HIGHLIGHTS

An exchange interaction-based single-molecule toroic named $\{Fe_8Dy_8\}$ is synthesized

The magnitude of exchange coupling for generating the toroidal moment is determined

The toroidal ground state is 4-fold degenerated, which is unprecedented in SMTs

The energy gap between the ground and the first excited states is determined by EPR

1 **Discovery**
A new material or phenomena

Zhang et al., Matter 2, 1481–1493
June 3, 2020
https://doi.org/10.1016/j.matt.2020.02.021

Matter

CellPress

Article

Single-Molecule Toroic Design through Magnetic Exchange Coupling

Hao-Lan Zhang,[1,4] Yuan-Qi Zhai,[1,4] Lei Qin,[1,4] Liviu Ungur,[2] Hiroyuki Nojiri,[3] and Yan-Zhen Zheng[1,5,*]

SUMMARY

Toroidal molecular magnets represent promising candidates for next-generation ultra-dense information storage. These wheel-like molecules are able to store one bit per molecule because of their insensitivity to homogeneous magnetic fields—one of the main sources of magnetic perturbations. However, synthesis of molecules possessing a well-defined and stable vortex arrangement of the on-site magnetic moments in the ground state represents a challenge. Here, we show that 16 magnetic metal ions can be alternately arranged into a macrocycle named {Fe_8Dy_8}. The net toroidal moment can be experimentally determined at 0.23 Tesla. Moreover, *ab initio* calculations were performed to reveal that ferromagnetic exchange interactions between the Fe^{III} and Dy^{III} metal centers are the key to generate this toroidal moment. This feature is significantly distinguished from the previously described dipole-dipole interaction-based single-molecule toroics (SMTs), showing the importance of exchange-coupling interactions in the design of next-generation SMTs.

INTRODUCTION

Vortex-like magnetic structures that combine both magnetic and topological orderings can generate toroidal magnetic moments,[1–3] which in principle simultaneously break time-reversal and space-inversion symmetries.[4] The spontaneous alignment of toroidal moments has long been discussed as ferrotoroidicity,[5–9] a source for the fourth form of ferroic order after ferromagnetism (spontaneous magnetization), ferroelectricity (spontaneous polarization), and ferroelasticity (spontaneous strain). In reality, this kind of ferroic order has long been pursued theoretically;[2] however, due to its weak response to the environment,[10,11] it was difficult to detect in traditional magnetic materials until the observation of ferrotoroidic domains in some metamaterials.[3,12] The search for the toroidal moment used to be limited to bulk materials, particularly in multiferroic materials, which are challenging to design and realize experimentally.[13]

In addition to these advances,[12–15] recently developed single-molecule toroics (SMTs), which show spin chirality and toroidal bistability associated with a non-magnetic ground state at the molecular level, are very attractive. Due to the variable metal ions and organic ligands, this system has more possibilities in designing and detecting toroidal moments. If the temperature is lower than the energy gap between the excited doublets and the ground state, the net toroidal magnetic moments of the SMTs can be completely blocked in the ground states, thereby protecting the bits information stored in them.[16] Moreover, ascribed to their inertness toward external homogeneous magnetic field, SMTs are promising for designing long-life spin-based qubits and ultra-high-density information storage

Progress and Potential

The big data era calls for larger capacity of our hard drive, which in turn depends on the number of magnetic units that store bits of 1 or 0. However, as the density of these units increases, flipping one unit without affecting another becomes more difficult because of undesired magnetic perturbations from the reading/writing heads. Single-molecule toroics (SMTs) that exploit vortex-like magnetic structures are insensitive to homogeneous magnetic fields and hence are promising for next-generation ultra-dense information storage. However, the synthesis of such molecular materials is challenging. Here, we show by using ferromagnetic interactions that this target can be realized in a 16-membered heterometallic cluster {Fe_8Dy_8}, which shows a stable 4-fold degenerated magnetic toroidal ground state at low temperatures. This is significantly distinguished from the most studied dipole-dipole interaction-based SMTs and demonstrates a promising strategy for the next generation of SMT design.

materials.[16–18] However, the molecular design for SMTs is very challenging, requiring the Ising-type on-site magnetic moments to be arranged in a vortex-like fashion from the proper molecular geometry and magnetic interactions.[11,13,19,20] Thus, the magnetic behavior of the first SMT, the $\{Dy_3\}$ triangle,[21] was initially defined as "unusual" until 2 years later, this "unusual" magnetic behavior was rationalized by theoretical calculations[22] and single-crystal experiments.[23] Both theory and experiments indicate that the $\{Dy_3\}$ triangle is interpreted within a non-collinear Ising model, together with a non-magnetic ground state and magnetic moments on the Dy^{III} sites that are in almost perfect toroidal distribution, and coupled by Ising exchange interaction, confirming the observation of SMT behavior.

Subsequently, several types of SMTs were identified in polynuclear Dy^{III} complexes with cyclic structures. Typical examples include various $\{Dy_3\}$ triangles,[24–27] coplanar $\{Dy_4\}$ squares,[28,29] $\{Dy_6\}$ hexagons,[30] and a unique $\{Dy_4\}$ cubane.[31] These examples all take the advantage of dipole-dipole interactions among the ground doublet states of the magnetically strong anisotropic Dy^{III} ions. However, according to Equation 1,

$$\tau \propto \sum_i r_i \times \tilde{s}_i, \qquad \text{(Equation 1)}$$

which defines the toroidal moment (τ) as the outer product of the displacement of the magnetic ions from the center position r_i and their ground pseudospin $\tilde{s}_i$ (pseudospin is equal to the true spin S_i in case of isotropic metals), to achieve larger τ needs larger r, $\tilde{s}_i$, and appropriate angles.[16] The strength of magnetic interactions (J_{ij}) between the ground pseudospins $\tilde{s}_i$ of interacting metal sites ($\propto \sum_i \sum_j J_{ij} \tilde{s}_i \tilde{s}_j$) sets the energy difference between the (ground) toroidal states and other (non-toroidal, excited) magnetic coupled states of the compound. The stronger are the magnetic interactions, the more stable is the toroidal magnetic state at higher temperatures. Hence, coupled $\{Dy_3\}$ triangles via exchange interactions through space or through 3d metal ions were developed to enhance τ.[27,32] In 2012, Powell et al. reported two structures of $(\{Cu^{II}Dy_3\}_n)$ 1D polymers and the observation of toroidal moments under applied magnetic field at low temperature. For the first time, this work introduced exchange coupling into the construction of new SMTs. In theory, two $\{Dy_3\}$ individually generate perfect toroidal moments in the ground state by dipole-dipole interactions while being connected to each other by exchange-coupling interactions via a Cu^{II} ion. Thus, $\{Cu^{II}Dy_3\}_n$ can be viewed as a field-induced SMT. More recently, Tang et al. also showed SMT behavior in a heterometallic $\{Cu^{II}{}_6Dy_6\}$ wheel, where six Cu^{II} and six Dy^{III} ions are arranged alternately and present magnetic exchange coupling between them, highlighting the importance of exchange-coupling interaction in constructing SMTs.[33] In addition to larger r and S, exchange-coupling interaction plays a significant role in enhancing τ, but the control of the molecular geometry and magnetic anisotropy in a large molecule becomes complicated. For instance, the $\{Mn^{III}{}_8Dy^{III}{}_8\}$[34] wheel does not show an obvious S-shaped magnetization plot, as the metal ions are weakly and antiferromagnetically coupled, and the magnetic anisotropy of the Mn^{III} ions ($3d^4$ and $S = 2$) are not favored to form the toroidal arrangement.

We reason that the replacement of the Mn^{III} ions with magnetically more isotropic Fe^{III} ($3d^5$ and $S = 5/2$) can reduce such a conflict and probably enhance the magnetic exchange-coupling interactions. Known Fe^{III}-4f wheel motifs include $\{Fe_4Dy_4\}$, $\{Fe_4Ln_2\}$, $\{Fe_5Yb_3\}$, $\{Fe_3Yb_2\}$, $\{Fe_{16}Ln_4\}$, and $\{Fe_{10}Ln_{10}\}$ complexes, all reported by Powell and coworkers.[35–40] Our recently developed solvothermal synthesis of Cr^{III}-rare earth (RE) wheel with the *N*-methyldiethanolamine ($mdeaH_2$) ligand allows us to

[1]Frontier Institute of Science and Technology (FIST), Xi'an Jiaotong University Shenzhen Research School, State Key Laboratory for Mechanical Behavior of Materials, MOE Key Laboratory for Nonequilibrium Synthesis of Condensed Matter, Xi'an Key Laboratory of Sustainable Energy and Materials Chemistry and School of Science, Xi'an Jiaotong University, 99 Yanxiang Road, Xi'an, Shaanxi 710054, China

[2]Department of Chemistry, National University of Singapore, Block S8 Level 3, 3 Science Drive 3, Singapore 117543, Singapore

[3]Institute of Materials Research (IMR), Tohoku University, Katahira, Sendai 980-8577, Japan

[4]These authors contributed equally

[5]Lead Contact

*Correspondence: zheng.yanzhen@xjtu.edu.cn

https://doi.org/10.1016/j.matt.2020.02.021

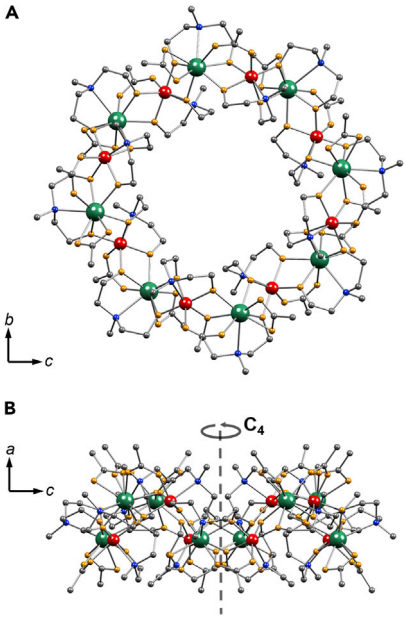

Figure 1. The Structure of {Fe_8Dy_8} Determined by X-Ray Crystallography

(A) A perspective view of the molecular structure of **1Dy**.

(B) The side view of **1Dy** and the C_4 axis highlighted by the dotted line.

Color codes: Fe, red; Dy, sea green; C, gray; N, blue; O, light orange. Solvent molecules and hydrogen atoms were omitted for clarity.

expand to the isocharged Fe^{III} system.[41] Herein, we show the 16-membered mixed Fe-RE macrocycle $[Fe_8Dy_8(mdea)_{16}(CH_3COO)_{16}]\cdot CH_3CN\cdot 18H_2O$ (**1Dy**) with a net toroidal moment precisely determined at 0.23 T by the combination study of magnetization, high-frequency/high-field electron paramagnetic resonance (HF-EPR) spectroscopy experiments, and *ab initio* calculations. Moreover, to elucidate the magnetic interaction in this giant molecular wheel, two analogous compounds, $[Fe_8Y_8(mdea)_{16}(CH_3COO)_{16}]\cdot 5CH_3CN\cdot 32H_2O$ (**1Y**) and $[Al_8Dy_8(mdea)_{16}(CH_3COO)_8(NO_3)_8]\cdot 2CH_3CN\cdot 9H_2O$ (**2Dy**), each with only one kind of homo-spin center, were also synthesized. A detailed comparison of the magnetic properties of these three compounds reveals that the ferromagnetic exchange interaction between the Fe^{III} and the Dy^{III} ions in **1Dy** is the key to show such a net toroidal moment. Our work also thoroughly interprets the correlation between the toroidal magnetization and the microstates by using *ab initio* calculations, the only proven way to deliver insight into this information to date.

RESULTS AND DISCUSSION

Crystal Structures

Compounds **1Dy** and **1Y** are isostructural and crystallize in the cubic space group of *Pn*-3*n* (Figure 1; see also Table S1). Here, only the structure of **1Dy** is described as a representative. In **1Dy**, eight Fe^{III} and eight Dy^{III} ions are circularly and alternately arranged to form a 16-membered wheel around the central C_4 symmetry. At the center of the wheel is a disordered acetonitrile, which lies exactly along the C_4 axis. Each Fe^{III} ion is six-coordinately bound to three 3.212 (in Harris notation[42]) $mdea^{2-}$ ligands (Figure S1) and one 2.11 acetate ligand; under solvothermal conditions the acetate is generated *in situ* from acetylacetone or acetonitrile, as reported previously.[43,44] For each Dy^{III} ion, the coordination mode is similar to the Fe^{III} sites in addition to a chelated 1.11 acetate ligand, forming the eight-coordinate environment (Figure S5). The Dy–O bond lengths are in the range of 2.29–2.44 Å while the Fe–O distances lie from 1.95 to 2.05 Å (Table S2). The Fe···Dy, Fe···Fe, and Dy···Dy separations in the wheel are in the range of 3.36–3.45 Å, 5.87–5.92 Å, and 6.20–6.32 Å, respectively. The shortest Dy···Dy distance between two adjacent

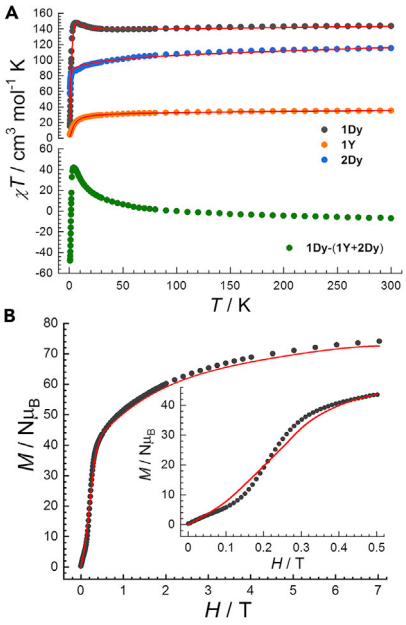

Figure 2. The Magnetic Characteristics of 1Dy, 1Y, and 2Dy

(A) Top: temperature-dependent dc magnetic susceptibility collected in an applied 1,000 Oe dc field from 0.5 to 300 K for **1Dy**, **1Y**, and **2Dy**. Bottom: subtraction of the experimental χT versus T data for **1Y** and **2Dy** from that of **1Dy**. The red solid lines are the POLY_ANISO fit of the data (for details, see the theoretical section).

(B) Field variation of the magnetization at 0.5 K and the calculated curve (red line). Inset: the magnified section at lower field variation of 0–0.5 T.

$\{Fe_8Dy_8\}$ rings is 9.21 Å while the shortest Fe···Fe distance is 9.45 Å (Figure S2). The separations between Dy···Dy and Fe···Fe centers from adjacent metal rings are, therefore, large enough to prevent any significant magnetic interactions between neighboring rings.

The substitution of Fe^{III} by Al^{III} gives **2Dy**, which is structurally very similar to **1Dy** but crystallizes in the orthorhombic space group *Fddd* (Figures S3 and S7; see also Table S1). The eight Al^{III} and eight Dy^{III} metal centers are also arranged alternately to form a 16-membered macrocycle. Similar to Fe^{III}, each Al^{III} ion is six-coordinate in the same cavity provided by the 3.212 $mdea^{2-}$ and 2.11 acetate ligands. However, because the ionic radius of Al^{III} is only 0.535 Å, which is distinctly smaller than that of the Fe^{III} ion (0.645 Å), the Al–O, Al···Dy, and Dy···Dy separations in **2Dy** are all shorter, leading to corresponding ranges of 1.84–1.91 Å, 3.28–3.38 Å, and 6.04–6.10 Å (Table S3). The molecules in **2Dy** are packed in an ABAB fashion with the shortest Dy···Dy separation of 8.93 Å between adjacent $\{Al_8Dy_8\}$ rings (Figure S4).

The major difference in the Dy environment between **1Dy** and **2Dy** is the peripheral coordinating ligands. For the former there is one 1.11 acetate while for the latter there is one 1.11 nitrate. Continuous symmetry measure (CSM) analysis using the program SHAPE (Table S4) indicates that the Dy^{III} ions in both **1Dy** and **2Dy** are eight-coordinate and in the distorted biaugmented trigonal prism (J50) coordination geometry, with the CSM value ranging from 22.9 to 25.5. Hence, the local coordination environments of the Dy^{III} ions in both **1Dy** and **2Dy** are indeed very similar (Figures S5 and S6).

Magnetic Properties

The temperature-dependent magnetic susceptibilities of **1Dy** and **1Y** polycrystalline samples were measured in the temperature range of 0.5–300 K under 1,000 Oe dc field. For **1Dy**, at room temperature the χT product of 143.6 $cm^3\ mol^{-1}\ K$ agrees well with the expected summation (148.3 $cm^3\ mol^{-1}\ K$) for eight Dy^{III} (S_{Dy} = 5/2, L_{Dy} = 5, g_{Dy} = 4/3) and eight Fe^{III} ions (S_{Fe} = 5/2, g_{Fe} = 2). Upon cooling, the χT

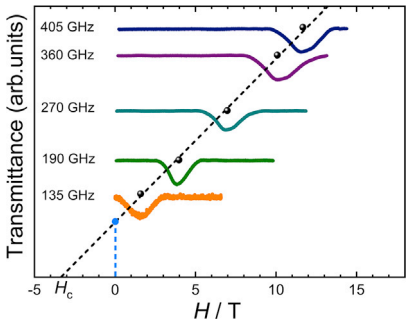

Figure 3. Selected HF-EPR Spectra of 1Dy Measured at 4.2 K

The black dashed line is the linear fitting of the data in the frequency-field plot. The blue dot represents the zero-field gap at 0 T.

product remains nearly constant down to 30 K, followed by an increase to a peak of 147.6 $cm^3\ mol^{-1}$ K at 6 K (Figure 2A). Thereafter a sharp decrease is observed, reaching the lowest value of 16.1 $cm^3\ mol^{-1}$ K at 0.5 K. The sharp decrease of the χT product toward a zero value implies a non-magnetic ground state. If we extrapolate the χT versus T plot to 0 K, this non-magnetic tendency is very obvious, which is one of the important features of SMTs. More specifically, the isothermal field-dependent magnetization plots (M versus H) at 0.5 K show an S shape at low fields. By taking the first derivative of the M versus H plot, the inflection point is determined to be 0.23 T. The magnetization finally reaches 74.4 μ_B at 7 T without saturation, indicating the presence of significant magnetic anisotropy (Figure 2B).

To elucidate the magnetic interaction of **1Dy**, the nature of the Fe^{III}-Dy^{III} interaction is determined by the comparison study of the homo-spin analogs, **1Y** and **2Dy** (Figure 2A). Subtraction of the χT versus T data for **1Y** from that of **1Dy** removes the contribution of paramagnetism of the Fe^{III} ions as well as the effect of the Fe^{III}-Fe^{III} interactions. Meanwhile, subtraction of the experimental χT versus T data for **2Dy** from that of **1Dy** removes the contribution from the paramagnetism of the Dy^{III} ions and the effect of the Dy^{III}-Dy^{III} interactions. Finally, only the nature of the Fe^{III}-Dy^{III} interaction is left in the difference plot (Figure 2B, bottom). The subtracted curve shows an unambiguous increasing tendency up to 4 K, which is solid evidence of the ferromagnetic nature of the pure Fe^{III}-Dy^{III} interaction.[45,46]

Alternating-current (ac) susceptibility measurement, as an effective method to investigate dynamics of the magnetization, was performed on all three complexes. For **1Dy** and **1Y**, the in-phase (χ') and out-of-phase (χ'') signals show frequency-independent behavior under both 0 and 1,000 Oe dc field (Figure S9), indicating no slow magnetic relaxation behaviors. However, **2Dy** shows slow magnetic relaxation behavior under 0 and 2,500 Oe dc field (Figure S10). The Cole-Cole plots of χ' versus χ'' from 3.36 to 7.81 K were plotted to quantify the relaxation time and the width of its distribution (Figure S11). Using the generalized Debye model, the fitting generates α values ranging from 0.22 to 0.51.[47] Evaluated from the relaxation time τ (Table S5), the linear plot of $\ln(\tau)$ versus $1/T$ was revealed, implying that an Orbach process is dominant over the measured temperature and frequency span. The linear fitting by using the Arrhenius law $\tau = \tau_0 \exp(U_{eff}/k_B T)$ affords an energy barrier U_{eff} of 10.6 K with a pre-exponential factor $\tau_0 = 3.05 \times 10^{-6}$ s.

HF-EPR Spectra

HF-EPR spectra of polycrystalline **1Dy** were collected in the frequency range of 135–405 GHz at 4.2 K. A series of single, broad absorption bands was observed. The peaks of the absorption bands shift to higher fields as frequencies increase (Figure 3)

due to the transition from the non-magnetic ground state to the first excited Kramers doublet (KD). The linear fitting of the plot obviously has a negative bias field from the normal Zeeman effect, yielding the level-crossing field H_c at −3.35 T.[48,49] The zero-field gap of 107 GHz (3.55 cm^{-1}) can be transformed directly to the magnetic exchange interaction between Dy^{III} and Fe^{III} ions. Since the Fe^{III} sites possess little magnetic anisotropy, the observed characteristic frequency-field relationship shows the presence of an internal exchange-bias field at the Dy^{III} sites. Therefore, for $\{Fe_8Dy_8\}$, the HF-EPR spectra precisely present a negative level-crossing field which proves the ferromagnetic interactions between Dy^{III} and Fe^{III} ions. The zero-field gap is the EPR absorption at zero field, which is defined as the transition from the ground $\left|\pm1,\pm1,\pm1,\pm1,\pm1,\pm1,\pm1,\pm1;\pm\frac{5}{2},\mp\frac{5}{2},\pm\frac{5}{2},\mp\frac{5}{2},\pm\frac{5}{2},\mp\frac{5}{2},\pm\frac{5}{2},\mp\frac{5}{2}\right\rangle$ state to the first excited $\left|\mp1,\pm1,\pm1,\pm1,\pm1,\pm1,\pm1,\pm1;\pm\frac{5}{2},\mp\frac{5}{2},\pm\frac{5}{2},\mp\frac{5}{2},\pm\frac{5}{2},\mp\frac{5}{2},\pm\frac{5}{2},\mp\frac{5}{2}\right\rangle$ state according to the relation: $\Delta E = 2J_{ex}\sum(J^z_{Dy}S_{Fe})$. The observed energy splitting is consistent with the *ab initio* calculated energy gap between ground and excited states in the Zeeman diagram (see below).

Ab Initio Calculations

Ab initio calculations were performed on the experimental structures of **1Dy**, **1Y**, and **2Dy** using the MOLCAS 8.0 computational package (see Supplemental Information for details).[50–53] For the sake of simplicity, we started from **2Dy**, which comprises four non-equivalent Dy(III) centers (Figure S15). The calculated *g* tensors for the lowest eight KDs are very anisotropic ($g_z \approx 20$) with a pure $|\pm15/2\rangle$ type (Table S12). The energy gaps between ground and first excited KDs range from 154 to 191 cm^{-1}. The directions of local anisotropy axes on the eight Dy centers form a closed circle in the Dy_8 plane with some tilting (Table S11), resulting in a toroidal component with magnetic moments of the Dy^{III} ions projected onto the plane of the wheel. Using the POLY_ANISO[54] program, the exchange/dipolar interactions between $Dy^{III}\cdots Dy^{III}$ pairs (J_1) can be computed. Using the Lines model, we define the Ising interaction with $\tilde{J}_i = 25\cos\phi_i \cdot J_i$, where J_i is the effective Heisenberg exchange interaction with local Dy^{III} spins (S = 5/2) by neglecting the orbital contribution; parameter $\tilde{J}_i$ describes the anisotropic non-collinear exchange interaction between ground pseudospins ($\tilde{s}_i$ = 1/2) on Dy sites; and ϕ_i is the angle between local Ising magnetic moments of neighboring Dy sites. For **2Dy**, $J = -0.01$ cm^{-1} simulates well for all magnetization data, which leads to 16 first excited states with $\tilde{J}_i$ ranging from ca. 0.01 to 0.03 cm^{-1} (Table S10). This is a very small energy splitting from exchange states compared with the energy gap between the first excited and ground states of single Dy^{III} ions (Tables S6–S9). Since the first excited states of all four single-ion Dy^{III} sites are much higher in energy (>150 cm^{-1}) compared with those from exchange couplings, it is safe to only account for the excited states in plotting the Zeeman diagram. As a result, the Zeeman spectrum (Figure S13) displays the evolution of the lowest exchange-coupled states in an applied magnetic field. As one can see, the ground state can be viewed as $|\pm\tau\rangle = |\pm1,\pm1,\pm1,\pm1,\pm1,\pm1,\pm1,\pm1\rangle$ with magnetic moment directions of eight Dy^{III} sites forming a clockwise or counterclockwise toroidal moment. This KD shows non-magnetic behavior in zero applied field, which is not even influenced by magnetic field. The first excited states correspond to reversal of the direction of magnetization on one of the eight Dy^{III} sites with 16 microstates, e.g., $|\mp1,\pm1,\pm1,\pm1,\pm1,\pm1,\pm1,\pm1\rangle$. The totality of states can be divided into four degenerate states due to the four non-equivalent Dy^{III} centers with energy splitting ranging from ca. 0.01 to 0.03 cm^{-1}. Contrary to the ground state, those excited states can be easily affected by the field and a level crossing

between ground state $|\pm\tau\rangle$, and the $|\mp1, \pm1, \pm1, \pm1, \pm1, \pm1, \pm1, \pm1\rangle$ state lies at a field of 0.022 T, which is too small to be observed at finite temperatures (Figure S19).

The anisotropy axes of eight Dy^{III} ions in **2Dy** were found to lie in a circle around the wheel, suggesting the possibility of net toroidal behavior. However, the relatively small energy separation from the ground KD to the excited ones results in a hidden S shape in low-field $M(H)$ plot (Figure S8, inset). Since the effective energy barriers derived from the relaxation times are several orders of magnitude larger than the spread of energy levels in **2Dy**, we conclude that the dynamic magnetic relaxation arises from the individual Dy^{III} sites rather than exchange-coupling interaction.

To estimate the Fe^{III}-Fe^{III} exchange, we have computed the magnetic exchange-coupling constants on the full structure of **1Y** (Figures S17 and S18) using broken-symmetry density functional theory calculations assisted by the ORCA 4.0 computational package (see Supplemental Information for full computational details). The D value for individual Fe^{III} ions indicates that there are two types of Fe^{III} sites; one shows a D value around -0.3 cm^{-1} for Fe1, Fe3, Fe5, and Fe7 and the other shows a D value around -0.15 cm^{-1} for Fe2, Fe4, Fe6, and Fe8 (Table S13). Besides, they both show a relatively large E/D ratio. The calculation yielded antiferromagnetic exchange interactions of Fe^{III}-Fe^{III}, with the J value estimated to be -0.1 cm^{-1}, and a very small intermolecular interaction (zJ = 0.003 cm^{-1}). The production of the Hamiltonian results in fine fits of the χT and magnetization data (Figures S8 and S14):

$$H = -\sum_{j=1\sim7} JS_jS_{j+1} + D\left(S_z^2 - \frac{1}{3}S(S+1)\right) + E\left(S_x^2 - S_y^2\right) + \mu_B g S \cdot B. \qquad \text{(Equation 2)}$$

Based on the above results, the magnetic properties of **1Dy** in microscopic scale can be resolved. Due to its C_4 symmetry, the calculation of single-ion electronic structure divides into two parts, namely **1Dy-1** and **1Dy-2** (Figure S16). The results of the calculations yield anisotropic g values for **1Dy-1** of g_x = 0.43, g_y = 1.21, and g_z = 18.16, whereas for **1Dy-2** they yield g_x = 0.58, g_y = 1.71, and g_z = 17.69 (Tables S14 and S15). The energy gap between the ground-state and the first-excited-state KDs are found to be 81 cm^{-1} and 62 cm^{-1} for **1Dy-1** and **1Dy-2**, respectively. The main anisotropy axes of the ground state are located inside the Fe_8Dy_8 plane, with some angles much larger than that of **2Dy** deviated away from the plane, as shown in Figure S12. However, due to the enforced C_4 symmetry, all the moment vectors can be compensated with each other and result in a non-magnetic ground state.

As the system size of **1Dy** is very large and has exceeded the maximum states of 50,000 exchange states for the POLY_ANISO program, calculations are performed with only half of the size of the wheel. Moreover, the Fe^{III} ions are treated as an absolutely isotropic ion with g = 2.0, while just the ground states of the Dy^{III} ions are accounted for. The exchange/dipolar interactions between Dy^{III}-Dy^{III} (J_1'), Fe^{III}-Fe^{III} (J_2'), and Fe^{III}-Dy^{III} (J_3') are considered. Due to the similar structures of **1Dy**, **1Y**, and **2Dy**, we take J_1' = -0.01 cm^{-1} and J_2' = -0.1 cm^{-1} from the calculation results from **2Dy** and **1Y**, respectively. Thus, the Fe^{III}-Dy^{III} coupling constant (J_3') for **1Dy** can be calculated as 0.4 cm^{-1}, which confirms that the magnetic interactions between the adjacent Fe^{III} and Dy^{III} ions are ferromagnetic. Considering these parameters, the reasonable fits of magnetic susceptibilities and molar magnetization are shown in Figure 2, which further predicts a vanishing susceptibility when temperature approaches 0 K. This result is comparable with other reported SMTs, such as $\{Dy_3\}$

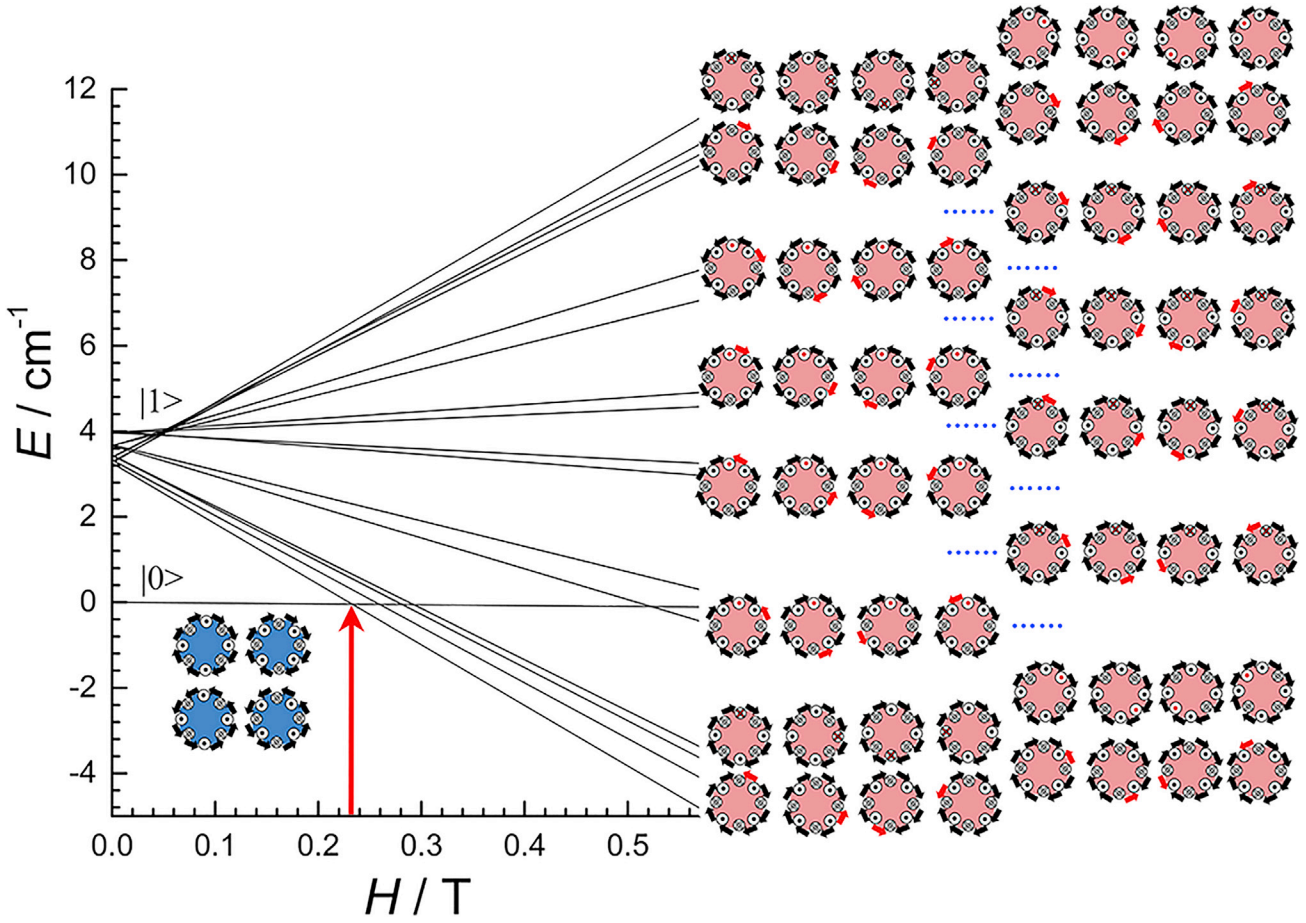

Figure 4. Energy Levels for 1Dy as Function of Magnetic Field (Zeeman Spectrum)

Schematic non-collinear magnetic structure of the ground states (blue) and the first excited states (pink) of **1Dy**. Red vertical arrow represents the level-crossing point at 0.23 T. The short arrows surrounding the circle are the local magnetic moments of Dy^{III} ions in the ground exchange doublet, in which red arrows represent the reversal of magnetization directions while the black ones represent original magnetization directions. The dots and crosses inside small white circles located between short arrows represent the in and out local magnetic moments of Fe^{III} ions vertical to the plane formed by the eight Dy sites, in which red dots and crosses represent the reversal of magnetization directions while the black ones represent original magnetization directions.

and $\{Dy_6\}$.[22,30] Thus, the strong intramolecular interaction between Fe^{III} and Dy^{III} is confirmed to be a relatively large stabilization energy of the toroidal state (ca. 3.4 cm^{-1}). The Zeeman diagram then can be drawn to create a visualized picture of the microstates of the ground state and the first excited states against the magnetic field. The ground state contains quadruple degenerate states with clockwise/anticlockwise anisotropic axes of Dy^{III} sites and the antiparallel oriented Fe^{III} sites, which can be viewed as $|\pm\tau;\pm\lambda\rangle = \left|\pm1,\ \pm1,\ \pm1,\ \pm1,\ \pm1,\ \pm1,\ \pm1,\ \pm1;\ \pm\frac{5}{2},\ \mp\frac{5}{2},\ \pm\frac{5}{2},\ \mp\frac{5}{2},\ \pm\frac{5}{2},\ \mp\frac{5}{2},\ \pm\frac{5}{2},\ \mp\frac{5}{2}\right\rangle$, where $|\pm\tau\rangle$ stands for clockwise (+) and anticlockwise (–) direction of Dy^{III} moment and $|\pm\lambda\rangle$ represents the in (+) and out (–) direction of the Fe^{III} sites (Figure 4). Meanwhile, the first excited state coming from the exchange coupling (ca. 3.4 cm^{-1} above the ground state) is much higher than that of **2Dy** (ca. 0.01 cm^{-1} above the ground state). There are three types of magnetization reversals contributing to the increased energy of the first excited state (1) the reversal of the magnetization on the Dy^{III} sites; (2) the reversal of the

magnetization on the Fe^{III} sites; and (3) the reversal of the magnetization on both Dy^{III} and Fe^{III} sites. The last type presents a larger energy splitting with more varied states than the previous two cases. All these degenerate excited states can be split by an applied field. At 0.23 T, there is a level crossing between the first excited states $\left|\mp 1, \pm 1, \pm 1, \pm 1, \pm 1, \pm 1, \pm 1, \pm 1; \pm\frac{5}{2}, \mp\frac{5}{2}, \pm\frac{5}{2}, \mp\frac{5}{2}, \pm\frac{5}{2}, \mp\frac{5}{2}, \pm\frac{5}{2}, \mp\frac{5}{2}\right\rangle$ and ground states, which leads to the observation of the S shape in the magnetization plot. All the low-lying microstates are illustrated in Figure 4, from which we can see that the first excited state corresponds to only one flip from either the Dy^{III} or the Fe^{III} sites. All other microstates are simply too high to contribute to the observed inflection point at 0.23 T in the magnetization plot.

DISCUSSION

Comparing **1Dy** with **2Dy**, the former presents an obvious S shape in magnetization plots at 0.5 K while the latter does not. The magnetic exchange interaction between the Fe^{III} and Dy^{III} ions in **1Dy** leads to an order-of-magnitude higher energy gap between the ground and the first excited state than that of **2Dy**. Therefore, a pronounced level crossing can be observed for **1Dy** up to 0.5 K (Figure 4). Hence, the insertion of Fe^{III} ions proves to be an effective strategy for stabilizing the ground state in SMTs, since the pure Dy^{III} complex, albeit having very strong magnetic anisotropy and high magnetic moment, generally exploits little exchange-coupling strength. For further enhancement of the toroidal moment, strong magnetic interaction between lanthanide centers is desired.[55]

Overall, we have successfully isolated three heterometallic clusters with vortex-like structures. The S-shaped behavior clearly observed in low-temperature magnetization plots at 0.5 K shows that **1Dy** contains a significant net toroidal moment. Further HF-EPR and theoretical analyses determine this net toroidal moment to be at 0.23 T, which is the first Fe-4f SMT whose toroidal moment is unambiguously determined. Comparison between **1Dy** and **2Dy** reveals that ferromagnetic exchange interaction of Fe^{III}-Dy^{III} contributes vitally to the large energy gap between the ground state and the first excited state in **1Dy**; hence, a pronounced level crossing results from it. Since magnetic exchange coupling can offer more options on ligand design, our work demonstrates a promising strategy for the next generation of SMT design.

EXPERIMENTAL PROCEDURES

Materials and Measurements

All reagents are commercially available and were used as received without further purification. Single-crystal X-ray diffraction data were recorded on a Bruker Apex DUO diffractometer with graphite-monochromated Mo Kα radiation (λ = 0.71073 Å). Absorption corrections were applied using a multiscan technique. Elemental analyses (C, H, and N) were performed on an EUROVECTOR EA3000 elemental analyzer. Infrared spectra (4,000–400 cm^{-1}) of all samples were recorded on a Thermo Scientific Nicolet 6700 FTIR spectrophotometer. Magnetic measurements (2–300 K) were carried out on powder samples by SQUID magnetometry (Quantum Design MPMS-XL). The data from 0.5 to 2.0 K were obtained on the *iHelium-3* accessory combined with MPMS-XL. Diamagnetic corrections were calculated from Pascal constants.

Synthesis

For **1Dy**, a mixture of $Fe(acac)_3$ (353 mg, 1 mmol), $Dy(NO_3)_3 \cdot 6H_2O$ (456 mg, 1 mmol), $mdeaH_2$ (357 mg, 3 mmol), and triethylamine (303 mg, 3 mmol) was stirred in

acetonitrile (8 mL) in air for 15 min. The slurry was then transferred into a 12-mL glass vial and heated at 130°C with auto-generous pressure for 72 h. Thereafter, the reactants were cooled to room temperature at a rate of 5°C/h. Dark-red and block-like crystals were isolated and washed with acetonitrile. Yield: 325 mg, 52.7% based on Dy. Elemental analysis (EA) (calcd., found): C (27.77, 27.69), H (5.38, 5.43), N (4.83, 4.79).

For **1Y**, the synthetic condition is similar to **1Dy**, except using $Y(NO_3)_3 \cdot 5H_2O$ (365 mg, 1 mmol) to replace $Dy(NO_3)_3 \cdot 5H_2O$. Yield: 313 mg, 52.6% based on Y. EA (calcd., found): C (30.79, 30.07), H (6.42, 6.06), N (6.18, 6.02).

For **2Dy**, a mixture of $Al(acac)_3$ (324 mg, 1 mmol), $Dy(NO_3)_3 \cdot 6H_2O$ (456 mg, 1 mmol), *N*-mdeaH_2 (357 mg, 3 mmol), and triethylamine (303 mg, 3 mmol) was stirred in acetonitrile (10 mL) in air for 15 min. The slurry was then transferred into a 15-mL Teflon-lined autoclave and heated at 150°C for 72 h. Thereafter, the reactants were cooled to room temperature at a rate of 5°C/h. Colorless block-like crystals were isolated and washed with cold acetonitrile. Yield: 117 mg, 20.3% based on Dy. EA (calcd., found): C (26.09, 26.39), H (4.90, 4.92), N (7.91, 7.14).

X-Ray Crystallography

Single-crystal X-ray diffraction data were collected on a Bruker Apex DUO diffractometer with Mo Kα radiation (λ = 0.71073 Å). Absorption corrections were applied using a multiscan technique. The structures were solved by direct method of SHELXTL and refined by full-matrix least-square techniques using the SHELXTL and OLEX2 programs. Severely disordered guest molecules, such as water and acetonitrile, were squeezed by PLATON software. Anisotropic thermal parameters were assigned to all non-hydrogen atoms. The hydrogen atoms were generated geometrically. Cambridge Crystallographic Data Center (CCDC) numbers 1942406–1942408 contain the crystallographic data for this paper. These data can be obtained free of charge via www.ccdc.cam.ac.uk/data_request/cif.

Computational Details

Ab initio calculations with state-average Complete-Active-Space-Self-Consistent Field (SA-CASSCF) and N-electron valence perturbation theory to second order were performed by using the ORCA 4.0 computational package for the Fe^{III} ion. The active space was composed of five 3d electrons and five 3d orbitals, namely CAS (5, 5), with 1 state for sextet, 24 states for quartet, and 75 states for doublet. The mean field approximation (SOMF) was used to account for the spin-orbit coupling. The basis set for iron and coordinated atoms was polarized triple-ζ-quality basis set (def2-TZVP), while the smaller basis set, def2-SVP, was used for the other remote atoms. Meanwhile, we also considered the scalar relativistic effects by including a standard second-order Douglas-Kroll-Hess for Fe^{III} center, and the auxiliary basis set def2/J was used in conjunction with the resolution of identity approximation.

The Fe-Fe exchange-coupling constant *J* was calculated using the following Hamiltonian by hybrid functional B3LYP with a TZVP basis set for all atoms:

$$\widehat{H}_{ex} = -\sum JS_{Fe}S_{Fe}. \qquad \text{(Equation 3)}$$

Ab initio calculations at SA-CASSCF/RASSI level were performed on program MOLCAS 8.0 and the structure was originally taken from the X-ray crystallographic result without optimization. The basis sets were chosen from the ANO-RCC library.

The Dy atom was treated with VTZP quality; Cl and O atoms were treated with VDZP quality; C and H atoms were treated with VDZ quality. The state-averaged CASSCF orbitals of the sextets, quartets, and doublets were optimized with 21, 224, and 490 states, respectively, using the RASSCF module. A total of 21, 128, and 130 sextets, quartets, and doublets, respectively, were chosen to construct and diagonalize the spin-orbit (SO) coupling Hamiltonian with the RASSI module. These obtained SO states were written into the SINGLE_ANISO[56] program to further compute the *g* tensors, crystal field parameters, and magnetic energy levels for the doublets of the ground $J = 15/2$ multiplet of the ^{6}H term for Dy^{III}. The two electron integrals were decomposed using the Cholesky method with a threshold of 1×10^{-8} to account for the accuracy. The exchange/dipolar interactions of Dy^{III}-Fe^{III} were computed by using POLY_ANISO. As the system size is very large and exceeds 50,000 exchange states of the limit of the POLY_ANISO program, calculations are simplified as described in the main text.

Calculation of Interactions

The exchange Hamiltonian adapted for complexes **1Dy**, **1Y**, and **2Dy** is

$$\widehat{H}_{ex} = -\sum_{i=1,2,3;j=1\sim8} J_i S_j S_{j+1}. \qquad \text{(Equation 4)}$$

Here, J_i represents the parameters of the magnetic exchange interaction between metal sites. The dipolar interactions between Dy^{III} ions were calculated on the basis of the local *g* tensors of the corresponding ground Kramers doublets obtained in *ab initio* calculations. The fitting is further performed by employing the following Hamiltonian, where the magnetic moments of all the ions and their corresponding distances are taken into consideration:

$$\widehat{H}_{dip} = \frac{\mu_0}{4\pi}\sum_{p,q}\left(\frac{M_p \cdot M_q}{|R_{pq}|^3} - 3\frac{(M_p \cdot R_{pq})(M_q \cdot R_{pq})}{|R_{pq}|^5}\right). \qquad \text{(Equation 5)}$$

The Hamiltonian describing the total magnetic interaction is a sum of exchange and dipole operators ($\widehat{H}_{total} = \widehat{H}_{ex} + \widehat{H}_{dip}$). Diagonalization of the $\widehat{H}_{total}$ gives the energy spectrum and the coupled eigenstates.

DATA AND CODE AVAILABILITY

All single-crystal data of **1Dy**, **1Y**, and **2Dy** have been deposited in the CCDC and can be downloaded free of charge from http://www.ccdc.cam.ac.uk/data_request/cif. The accession numbers are CCDC: 1942406, 1942407, and 1942408, respectively.

SUPPLEMENTAL INFORMATION

Supplemental Information can be found online at https://doi.org/10.1016/j.matt.2020.02.021.

ACKNOWLEDGMENTS

This work was supported by the Natural Science Foundation of China (nos. 21773130 and 21971203), Shenzhen Science and Technology Program (JCYJ20180306170859634), State Key Laboratory for Mechanical Behavior of Materials (20182006), Key Laboratory Construction Program of Xi'an Municipal Bureau of Science and Technology (201805056ZD7CG40), Cyrus Chung Ying Tang Foundation, Fundamental Research Funds for the Central Universities, and GIMRT program of Tohoku University. We also thank Mr. Gang Chang at the Instrument Analysis Center of Xi'an Jiaotong University for his assistance with elemental analysis. The scientific grants R-143-000-A80-114 and

R-143-000-A65-133 from the National University of Singapore are gratefully acknowledged. Computational resources from NSCC (ASPIRE-1, grant 11001278) were used for this study.

AUTHOR CONTRIBUTIONS

Y.-Z.Z. designed and directed the project. H.-L.Z. and L.Q. carried out the synthesis and most of the characterization. Y.-Q.Z. and L.U. carried out the detailed *ab initio* calculations. H.N. measured the low-temperature HF-EPR magnetic data. H.-L.Z., Y.-Q.Z., L.Q., L.U., and Y.-Z.Z. wrote the manuscript. All authors contributed to important discussions and suggestions on the manuscript.

DECLARATION OF INTERESTS

The authors declare no competing interests.

Received: November 5, 2019
Revised: December 24, 2019
Accepted: February 25, 2020
Published: March 18, 2020

REFERENCES

1. Van Aken, B.B., Rivera, J.-P., Schmid, H., and Fiebig, M. (2007). Observation of ferrotoroidic domains. Nature *449*, 702–705.
2. Dubovik, V.M., and Tugushev, V.V. (1990). Toroid moments in electrodynamics and solid-state physics. Phys. Rep. *187*, 145–202.
3. Fiebig, M. (2005). Revival of the magnetoelectric effect. J. Phys. D Appl. Phys. *38*, R123–R152.
4. Ascher, E. (1966). Some properties of spontaneous currents. Helv. Phys. Acta *39*, 40–48.
5. Yamaguchi, Y., and Kimura, T. (2013). Magnetoelectric control of frozen state in a toroidal glass. Nat. Commun. *4*, 2063–2067.
6. Gorbatsevich, A.A., and Kopaev, Y.V. (1994). Toroidal order in crystals. Ferroelectrics *161*, 321–334.
7. Sannikov, D.G. (1998). Ferrotoroic phase transition in boracites. Ferroelectrics *219*, 177–181.
8. Schmid, H. (2001). On ferrotoroidics and electrotoroidic, magnetotoroidic and piezotoroidic effects. Ferroelectrics *252*, 41–50.
9. Rabe, K.M. (2007). Response with a twist. Nature *449*, 674–675.
10. Dong, Z.-G., Zhu, J., Rho, J., Li, J.-Q., Lu, C., Yin, X., and Zhang, X. (2012). Optical toroidal dipolar response by an asymmetric double-bar metamaterial. Appl. Phys. Lett. *101*, 144105.
11. Spaldin, N.A., Fiebig, M., and Mostovoy, M. (2008). The toroidal moment in condensed-matter physics and its relation to the magnetoelectric effect. J. Phys. Condens. Matter *20*, 434203.
12. Kaelberer, T., Fedotov, V.A., Papasimakis, N., Tsai, D.P., and Zheludev, N.I. (2010). Toroidal dipolar response in a metamaterial. Science *330*, 1510–1512.
13. Ederer, C., and Spaldin, N.A. (2007). Towards a microscopic theory of toroidal moments in bulk periodic crystals. Phys. Rev. B Condens. Matter Mater. Phys. *76*, 214404.
14. Gnewuch, S., and Rodriguez, E.E. (2019). The fourth ferroic order: current status on ferrotoroidic materials. J. Solid State Chem. *271*, 175–190.
15. Tolédano, P., Ackermann, M., Bohatý, L., Becker, P., Lorenz, T., Leo, N., et al. (2015). Primary ferrotoroidicity in antiferromagnets. Phys. Rev. B *92*, 94431.
16. Ungur, L., Lin, S.-Y., Tang, J., and Chibotaru, L.F. (2014). Single-molecule toroics in Ising-type lanthanide molecular clusters. Chem. Soc. Rev. *43*, 6894–6905.
17. Sanvito, S. (2010). The rise of spinterface science. Nat. Phys. *6*, 562–564.
18. Cornia, A., and Seneor, O. (2017). The molecular way. Nat. Mater. *16*, 505–506.
19. Plokhov, D.I., Zvezdin, A.K., and Popov, A.I. (2011). Macroscopic quantum dynamics of toroidal moment in Ising-type rare-earth clusters. Phys. Rev. B *83*, 184415.
20. Schmid, H. (2008). Some symmetry aspects of ferroics and single phase multiferroics. J. Phys. Condens. Matter *20*, 434201.
21. Tang, J., Hewitt, I., Madhu, N.T., Chastanet, G., Wernsdorfer, W., Anson, C.E., Benelli, C., Sessoli, R., and Powell, A.K. (2006). Dysprosium triangles showing single-molecule magnet behavior of thermally excited spin states. Angew. Chem. Int. Ed. *45*, 1729–1733.
22. Chibotaru, L.F., Ungur, L., and Soncini, A. (2008). The origin of nonmagnetic Kramers doublets in the ground state of dysprosium triangles: evidence for a toroidal magnetic moment. Angew. Chem. Int. Ed. *47*, 4126–4129.
23. Luzon, J., Bernot, K., Hewitt, I.J., Anson, C.E., Powell, A.K., and Sessoli, R. (2008). Spin chirality in a molecular dysprosium triangle: the archetype of the noncollinear Ising model. Phys. Rev. Lett. *100*, 247205.
24. Ungur, L., Heuvel, W.V.d., and Chibotaru, L.F. (2009). *Ab initio* investigation of the non-collinear magnetic structure and the lowest magnetic excitations in dysprosium triangles. New J. Chem. *33*, 1224–1230.
25. Hewitt, I.J., Tang, J., Madhu, N.T., Anson, C.E., Lan, Y., Luzon, J., Etienne, M., Sessoli, R., and Powell, A.K. (2010). Coupling Dy_3 triangles enhances their slow magnetic relaxation. Angew. Chem. Int. Ed. *49*, 6352–6356.
26. Li, X.-L., Wu, J., Tang, J., Guennic, B.L., Shi, W., and Cheng, P. (2016). A planar triangular Dy_3 + Dy_3 single-molecule magnet with a toroidal magnetic moment. Chem. Commun. *52*, 9570–9573.
27. Lin, S.-Y., Wernsdorfer, W., Ungur, L., Powell, A.K., Guo, Y.-N., Tang, J., Zhao, L., Chibotaru, L.F., and Zhang, H.-J. (2012). Coupling Dy_3 triangles to maximize the toroidal moment. Angew. Chem. Int. Ed. *51*, 12767–12771.
28. Guo, P.-H., Liu, J.-L., Zhang, Z.-M., Ungur, L., Chibotaru, L.F., Leng, J.-D., Guo, F.-S., and Tong, M.-L. (2012). The first {Dy_4} single-molecule magnet with a toroidal magnetic moment in the ground state. Inorg. Chem. *51*, 1233–1235.
29. Gusev, A., Herchel, R., Nemec, I., Shul'gin, V., Eremenko, I.L., Lyssenko, K., Linert, W., and Trávníček, Z. (2016). Tetranuclear lanthanide complexes containing a hydrazone-type ligand. Dysprosium [2 × 2] gridlike single-molecule magnet and toroic. Inorg. Chem. *55*, 12470–12476.
30. Ungur, L., Langley, S.K., Hooper, T.N., Moubaraki, B., Brechin, E.K., Murray, K.S., and Chibotaru, L.F. (2012). Net toroidal magnetic moment in the ground state of a {Dy_6}-triethanolamine ring. J. Am. Chem. Soc. *134*, 18554–18557.

31. Garcia, G.F., Guettas, D., Montigaud, V., Larini, P., Sessoli, R., Totti, F., Cador, O., Pilet, G., and Guennic, B.L. (2018). A Dy_4 cubane: a new member in the single-molecule toroics family. Angew. Chem. Int. Ed. *57*, 17089–17093.

32. Vignesh, K.R., Soncini, A., Langley, S.K., Wernsdorfer, W., Murray, K.S., and Rajaraman, G. (2017). Ferrotoroidic ground state in a heterometallic $\{Cr^{III}Dy^{III}_6\}$ complex displaying slow magnetic relaxation. Nat. Commun. *8*, 1023.

33. Wu, J., Li, X.-L., Guo, M., Zhao, L., Zhang, Y.-Q., and Tang, J. (2018). Realization of toroidal magnetic moments in heterometallic 3d-4f metallocycles. Chem. Commun. *54*, 1065–1068.

34. Vignesh, K.R., Langley, S.K., Moubaraki, B., Murray, K.S., and Rajaraman, G. (2015). Large hexadecametallic $\{Mn^{III}$-$Ln^{III}\}$ wheels: synthesis, structural, magnetic, and theoretical characterization. Chem. Eur. J. *21*, 16364–16369.

35. Schray, D., Abbas, G., Lan, Y., Mereacre, V., Sundt, A., Dreiser, J., Waldmann, O., Kostakis, G.E., Anson, C.E., and Powell, A.K. (2010). Combined magnetic susceptibility measurements and ^{57}Fe Mössbauer spectroscopy on a ferromagnetic $\{Fe^{III}_4Dy_4\}$ ring. Angew. Chem. Int. Ed. *49*, 5185–5188.

36. Schmidt, S., Prodius, D., Novitchi, G., Kostakis, G.E., and Powell, A.K. (2012). Ferromagnetic heteronuclear $\{Fe_4(Er,Lu)_2\}$ cyclic coordination clusters based on ferric wheels. Chem. Commun. *48*, 9825–9827.

37. Baniodeh, A., Anson, C.E., and Powell, A.K. (2013). Ringing the changes in Fe^{III}/Yb^{III} cyclic coordination clusters. Chem. Sci. *4*, 4354–4361.

38. Baniodeh, A., Hewitt, I.J., Mereacre, V., Lan, Y., Novitchi, G., Anson, C.E., and Powell, A.K. (2011). Heterometallic 20-membered $\{Fe_{16}Ln_4\}$ (Ln = Sm, Eu, Gd, Tb, Dy, Ho) metallo-ring aggregates. Dalton Trans. *40*, 4080–4086.

39. Baniodeh, A., Liang, Y., Anson, C.E., Magnani, N., Powell, A.K., Unterreiner, A., Seyfferle, S., Slota, M., Dressel, M., Bogani, L., and Goß, K. (2014). Unraveling the influence of lanthanide ions on intra- and inter-molecular electronic processes in $Fe_{10}Ln_{10}$ nano-toruses. Adv. Funct. Mater. *24*, 6280–6290.

40. Machado, J.R., Baniodeh, A., Powell, A.K., Luy, B., Krämer, S., and Guthausen, G. (2014). Nuclear magnetic resonance relaxivities: investigations of ultrahigh-spin lanthanide clusters from 10 MHz to 1.4 GHz. ChemPhysChem *15*, 3608–3613.

41. Qin, L., Singleton, J., Chen, W.-P., Nojiri, H., Engelhardt, L., Winpenny, R.E.P., and Zheng, Y.-Z. (2017). Quantum Monte Carlo simulations and high-field magnetization studies of antiferromagnetic interactions in a giant hetero-spin ring. Angew. Chem. Int. Ed. *56*, 16571–16574.

42. Coxall, R.A., Harris, S.G., Henderson, D.K., Parsons, S., Tasker, P.A., and Winpenny, R.E.P. (2000). Inter-ligand reactions: *in situ* formation of new polydentate ligands. J. Chem. Soc. Dalton Trans. 2349–2356.

43. Kuhlman, R., Schimek, G.L., and Kolis, J.W. (1999). An extended solid from the solvothermal decomposition of $Co(Acac)_3$: structure and characterization of $Co_5(OH)_2(O_2CCH_3)_8 \cdot 2H_2O$. Inorg. Chem. *38*, 194–196.

44. Thiele, G., Wagner, B., and Dehnen, S. (2015). Solvothermal reactions in and with nitriles. Eur. J. Inorg. Chem. *2015*, 5329–5334.

45. Feltham, H.L.C., Clérac, R., Powell, A.K., and Brooker, S. (2011). A tetranuclear, macrocyclic 3d-4f complex showing single-molecule magnet behavior. Inorg. Chem. *50*, 4232–4234.

46. Dhers, S., Feltham, H.L.C., Rouzières, M., Clérac, R., and Brooker, S. (2019). Discrete versus chain assembly: hexacyanometallate linkers and macrocyclic {3d–4f} single-molecule magnet building blocks. Inorg. Chem. *58*, 5543–5554.

47. Guo, Y.N., Xu, G.F., Guo, Y., and Tang, J. (2011). Relaxation dynamics of dysprosium(III) single molecule magnets. Dalton Trans. *40*, 9953–9963.

48. Shimada, T., Okazawa, A., Kojima, N., Yoshii, S., Nojiri, H., and Ishida, T. (2011). Ferromagnetic exchange couplings showing a chemical trend in Cu-Ln-Cu complexes (Ln = Gd, Tb, Dy, Ho, Er). Inorg. Chem. *50*, 10555–10557.

49. Watanabe, R., Fujiwara, K., Okazawa, A., Tanaka, G., Yoshii, S., Nojiri, H., and Ishida, T. (2011). Chemical trend of Ln-M exchange couplings in heterometallic complexes with Ln = Gd, Tb, Dy, Ho, Er and M = Cu, V. Chem. Commun. *47*, 2110–2112.

50. Aquilante, F., Autschbach, J., Carlson, R.K., Chibotaru, L.F., Delcey, M.G., Vico, L.D., Galván, I.F., Ferré, N., Frutos, L.M., Gagliardi, L., et al. (2016). MOLCAS 8: new capabilities for multiconfigurational quantum chemical calculations across the periodic table. J. Comput. Chem. *37*, 506–541.

51. Ding, Y.-S., Chilton, N.F., Winpenny, R.E.P., and Zheng, Y.-Z. (2016). On approaching the limit of molecular magnetic anisotropy: a near-perfect pentagonal bipyramidal dysprosium(III) single-molecule magnet. Angew. Chem. Int. Ed. *55*, 16071–16074.

52. Ding, Y.-S., Yu, K.-X., Reta, D., Ortu, F., Winpenny, R.E.P., Zheng, Y.-Z., and Chilton, N.F. (2018). Field- and temperature-dependent quantum tunnelling of the magnetisation in a large barrier single-molecule magnet. Nat. Commun. *9*, 3134.

53. Liu, B.-C., Ge, N., Zhai, Y.-Q., Zhang, T., Ding, Y.-S., and Zheng, Y.-Z. (2019). An imido ligand significantly enhances the effective energy barrier of dysprosium(III) single-molecule magnets. Chem. Commun. *55*, 9355–9358.

54. Chibotaru, L.F., and Ungur, L. (2006). Program POLY_ANISO (University of Leuven).

55. Rinehart, J.D., Fang, M., Evans, W.J., and Long, J.R. (2011). Strong exchange and magnetic blocking in N_2^{3-}-radical-bridged lanthanide complexes. Nat. Chem. *3*, 538–542.

56. Roos, B.O., Lindh, R., Malmqvist, P.-Å., Veryazov, V., and Widmark, P.-O. (2005). New relativistic ANO basis sets for actinide atoms. Chem. Phys. Lett. *409*, 295–299.

Matter, Volume *2*

Supplemental Information

Single-Molecule Toroic Design through Magnetic Exchange Coupling

Hao-Lan Zhang, Yuan-Qi Zhai, Lei Qin, Liviu Ungur, Hiroyuki Nojiri, and Yan-Zhen Zheng

Supplemental Information

I. Supplemental Figures

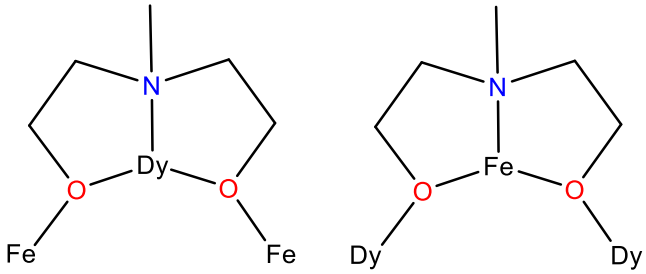

3.212 3.212

Figure S1. The two kinds of 3.212 (Harris notation) coordination modes of $mdea^{2-}$ in compounds **1Dy**. Harris notation describes the binding mode as $[X.Y_1Y_2Y_3. . .Y_n]$, where X is the overall number of metals bound by the whole ligand, and each value of Y refers to the number of metal atoms attached to the different donor atoms. See Coxall, R. A. *et al*. *J. Chem. Soc., Dalton Trans.* 2349–2356 (2000).

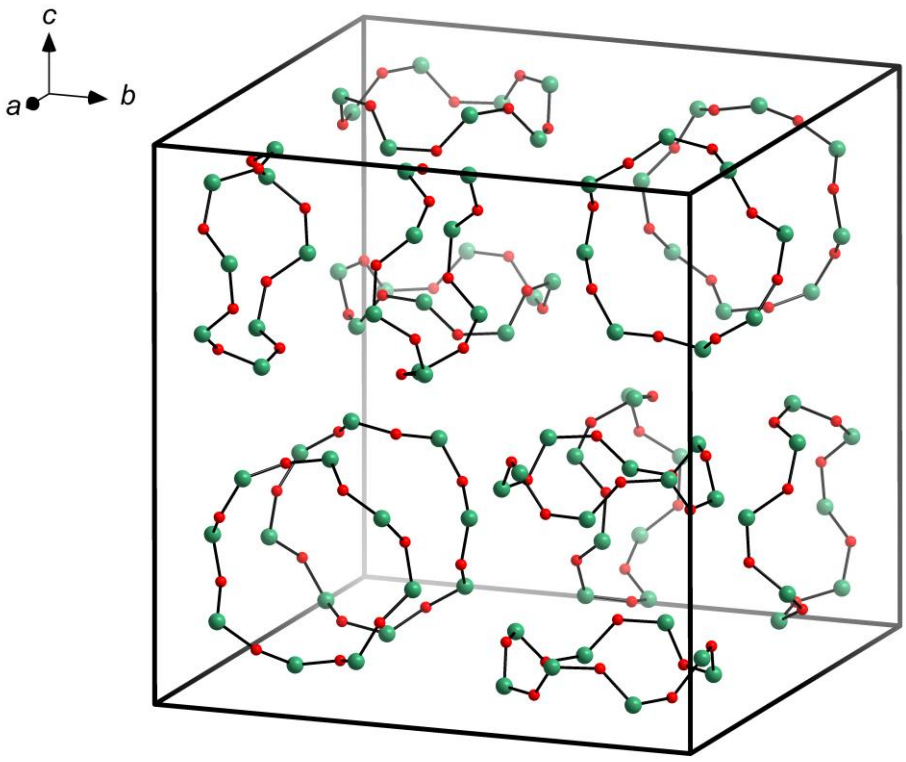

Figure S2. Molecular packing in unit cell of **1Dy**. Color codes: Fe, red; Dy, sea green. The non-metallic atoms were omitted for clarity.

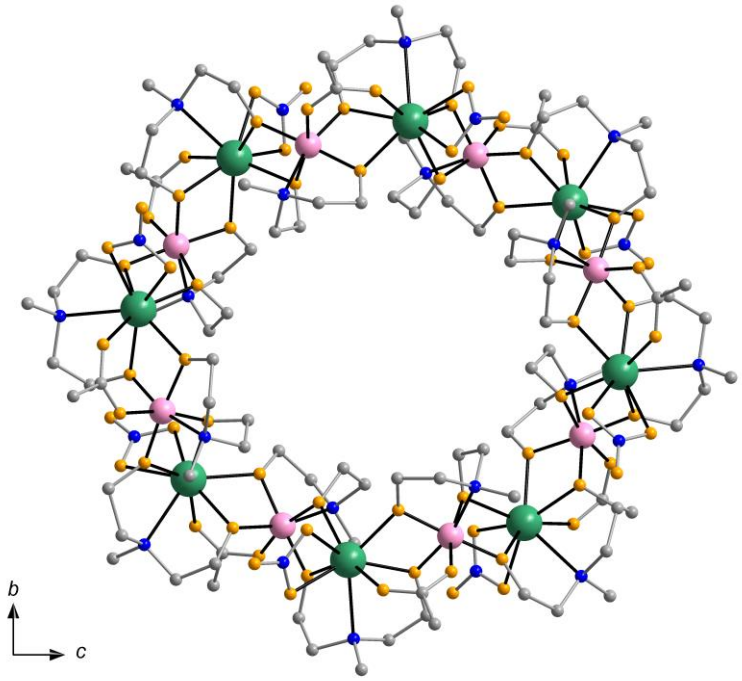

Figure S3. The molecular structure of complex **2Dy**. Color codes: Al, rose; Dy, sea green; C, grey; N, blue; O, light orange. The solvent molecules and hydrogen atoms were omitted for clarity. The Dy−O distances are ranging from 2.28 to 2.48 Å. The Dy−N (from $mdea^{2-}$) distances are in the range of 2.57 - 2.88 Å.

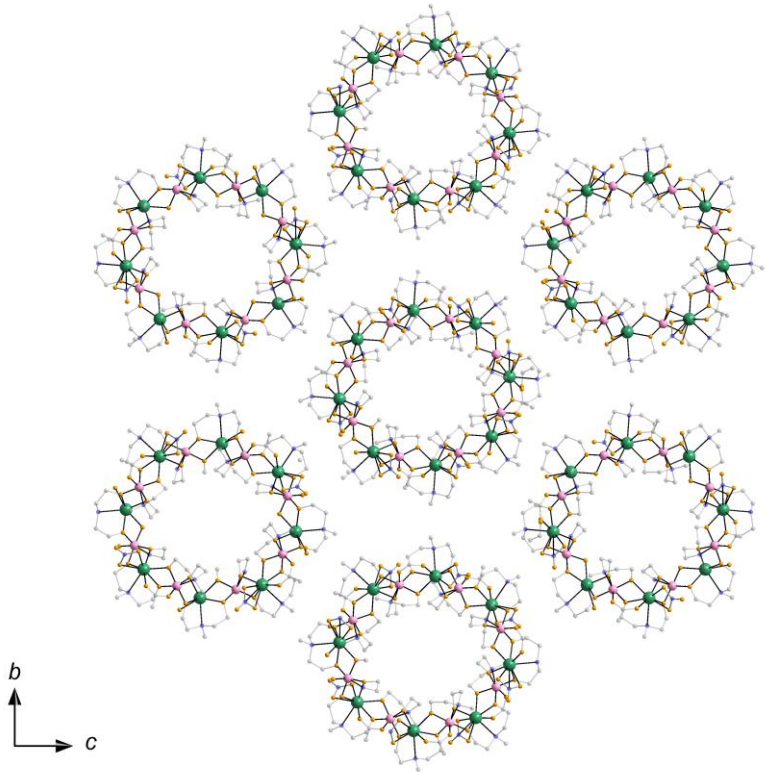

Figure S4. Molecular packing of complex **2Dy**. Color codes: Al, rose; Dy, sea green; C, grey; N, blue; O, light orange. The hydrogen atoms were omitted for clarity.

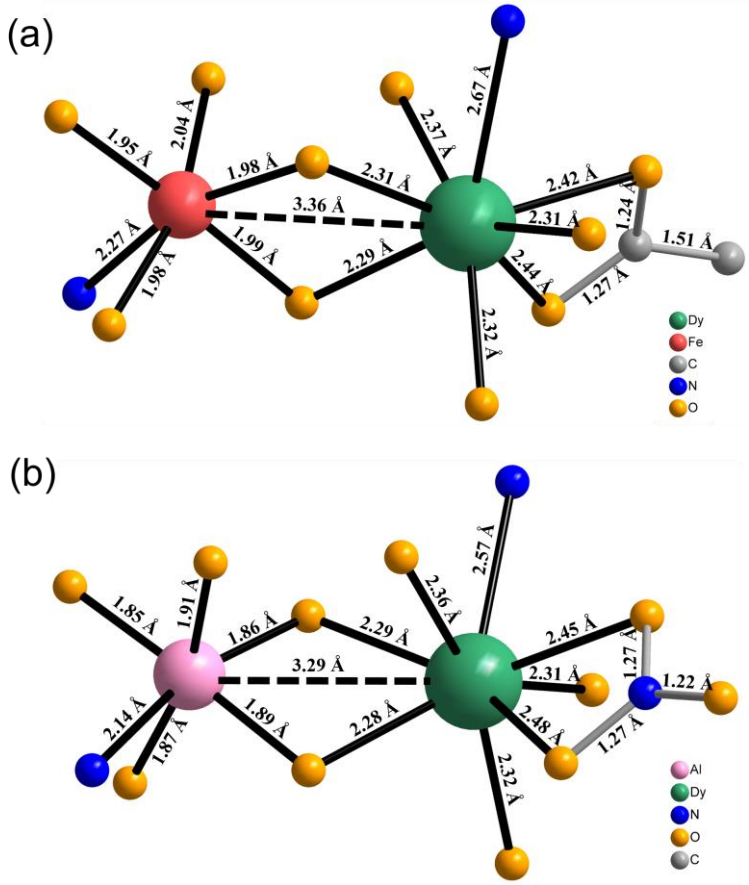

Figure S5. Local coordination environment of complexes **1Dy** (a) and **2Dy** (b).

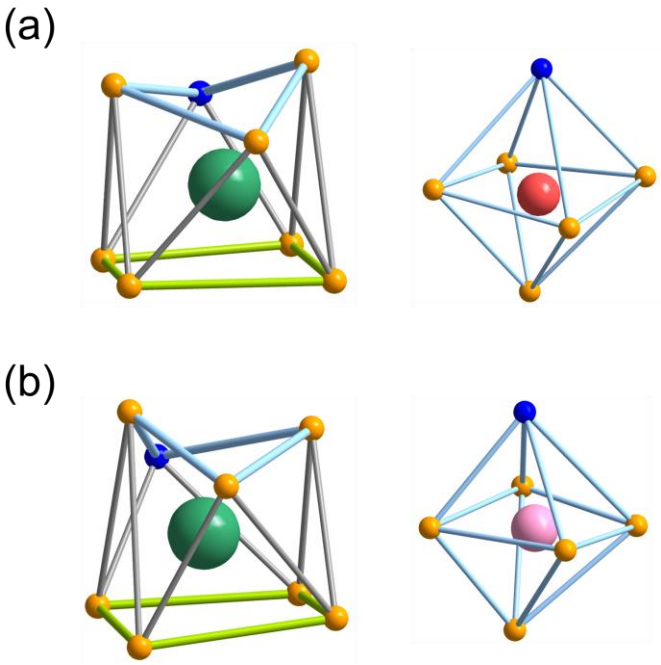

Figure S6. Coordination mode on metal centers of **1Dy** (a) and **2Dy** (b). Fe, red; Al, rose; Dy, sea green; N, blue; O, light orange.

(a)

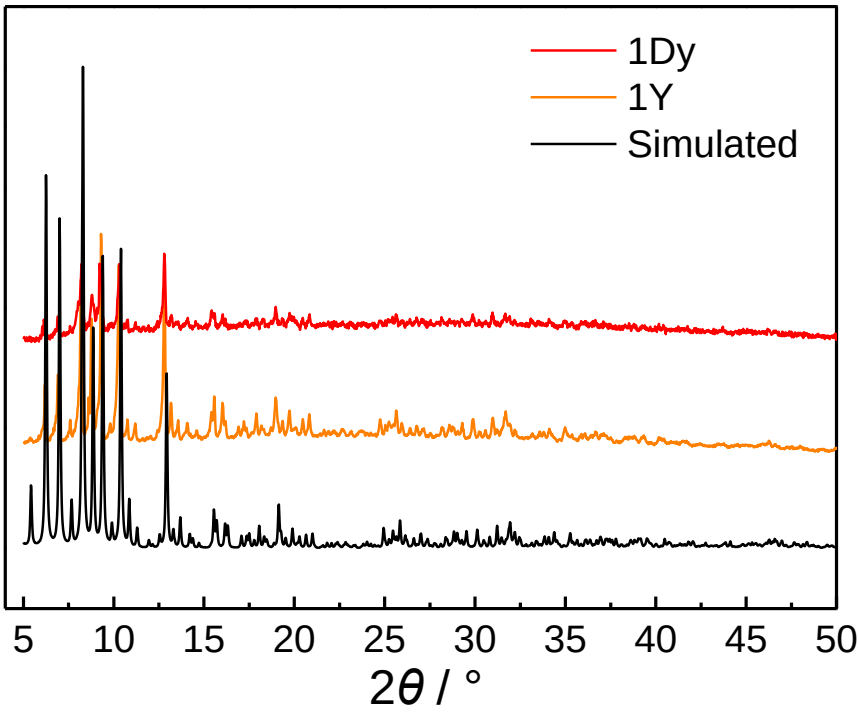

(b)

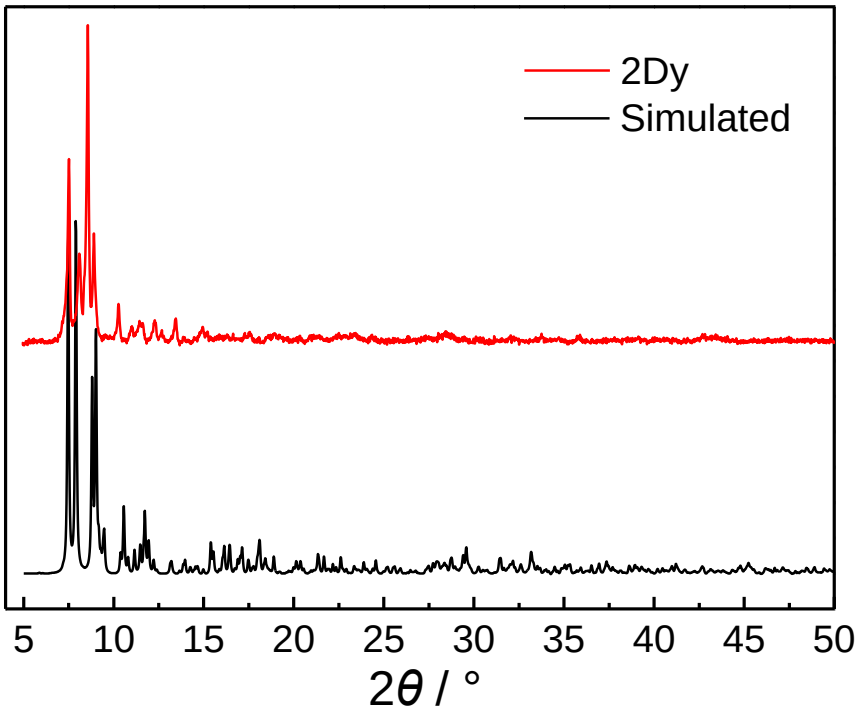

Figure S7. PXRD spectra for **1Dy** and **1Y** (a) and **2Dy** (b).

(a)

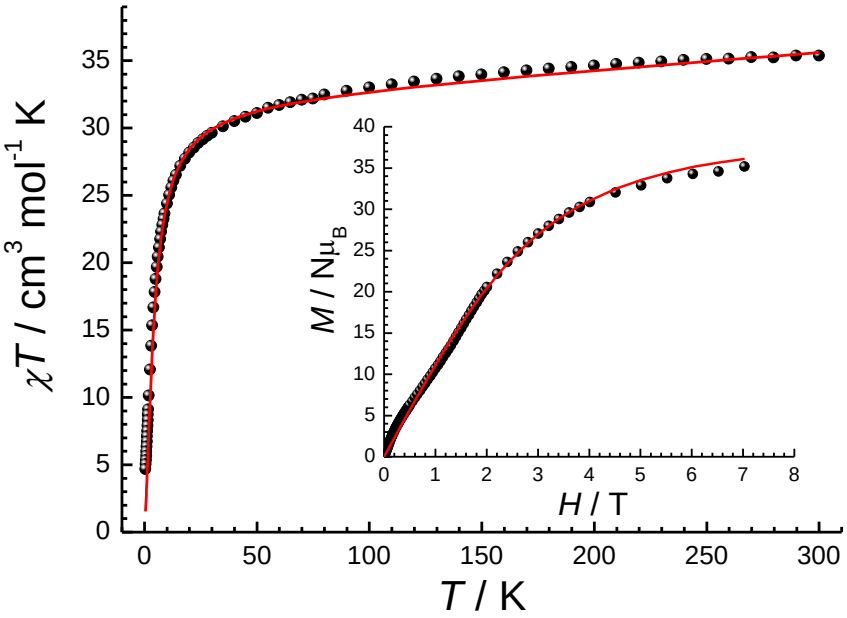

(b)

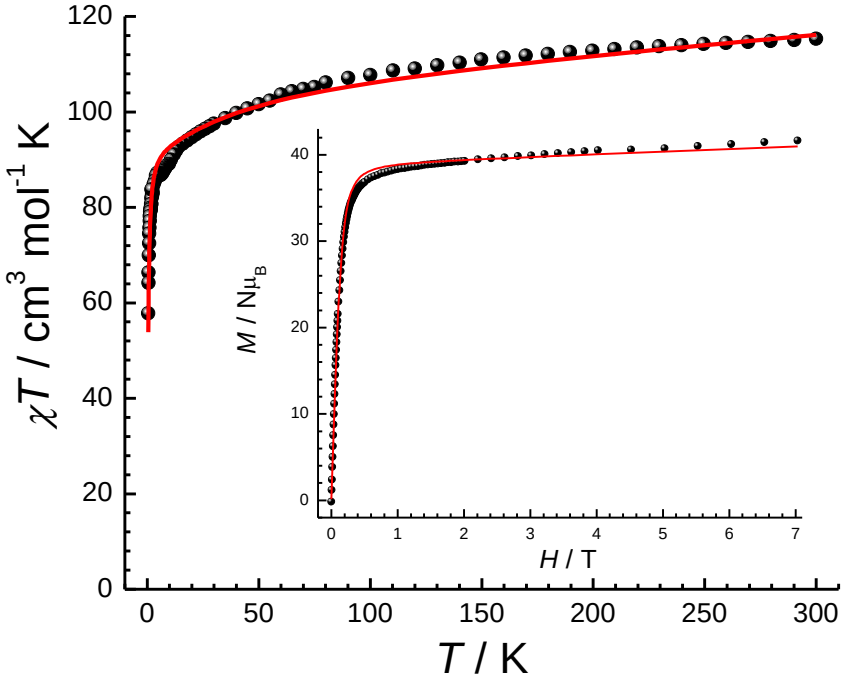

Figure S8. Temperature-dependent dc magnetic susceptibility plots of **1Y** from 0.5 to 300 K under 1000 Oe dc field. The red solid lines are BS-DFT fits of the data. Inset: Field-dependent magnetization plots at 0.5 K (a); Temperature-dependent dc magnetic susceptibility plots of **2Dy** from 0.5 to 300 K under 1000 Oe dc field. The red solid lines are POLY_ANISO fits of the data. Inset: Field-dependent magnetization plots at 0.5 K (b) .

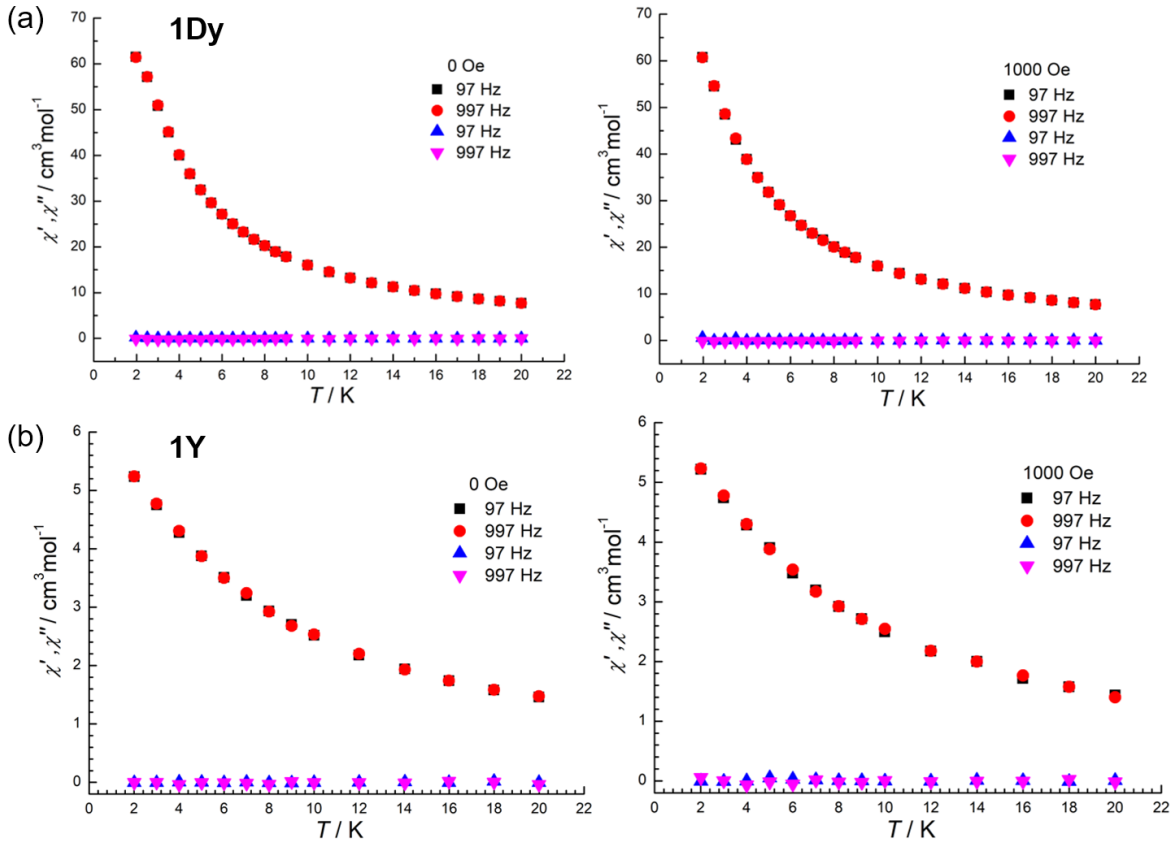

Figure S9. Temperature dependence of the ac susceptibilities for **1Dy** (a) and **1Y** (b) at the indicated frequencies under 0 Oe and 1000 Oe dc fields.

(a)

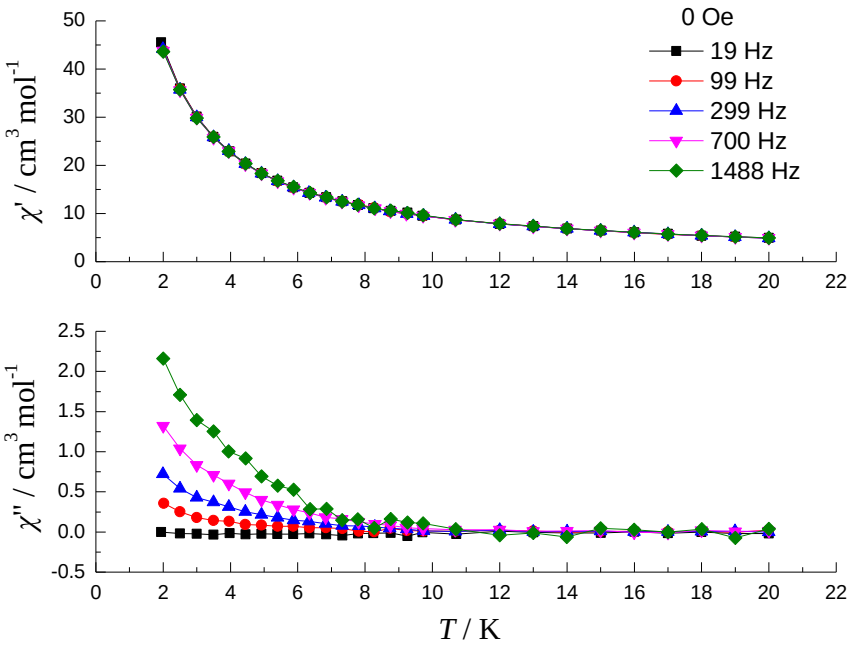

(b)

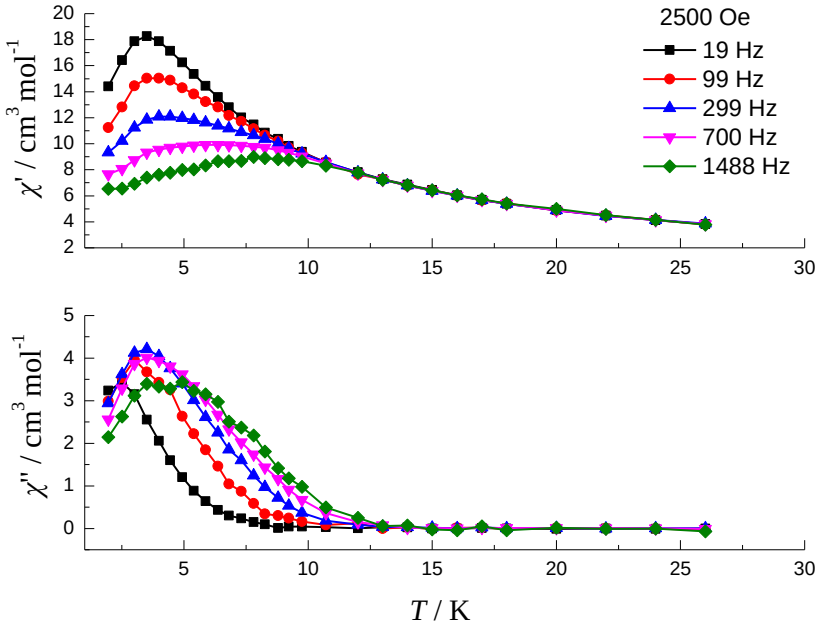

Figure S10. Ac magnetic susceptibility signals for **2Dy** under 0 Oe (a) and 2500 Oe (b) dc field at the indicated frequencies.

(a)

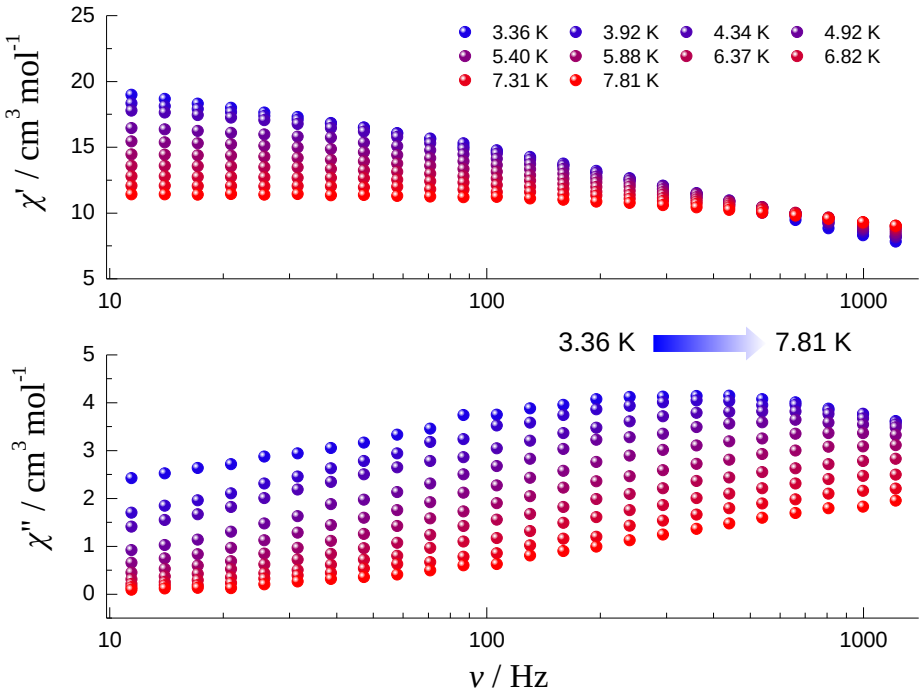

(b)

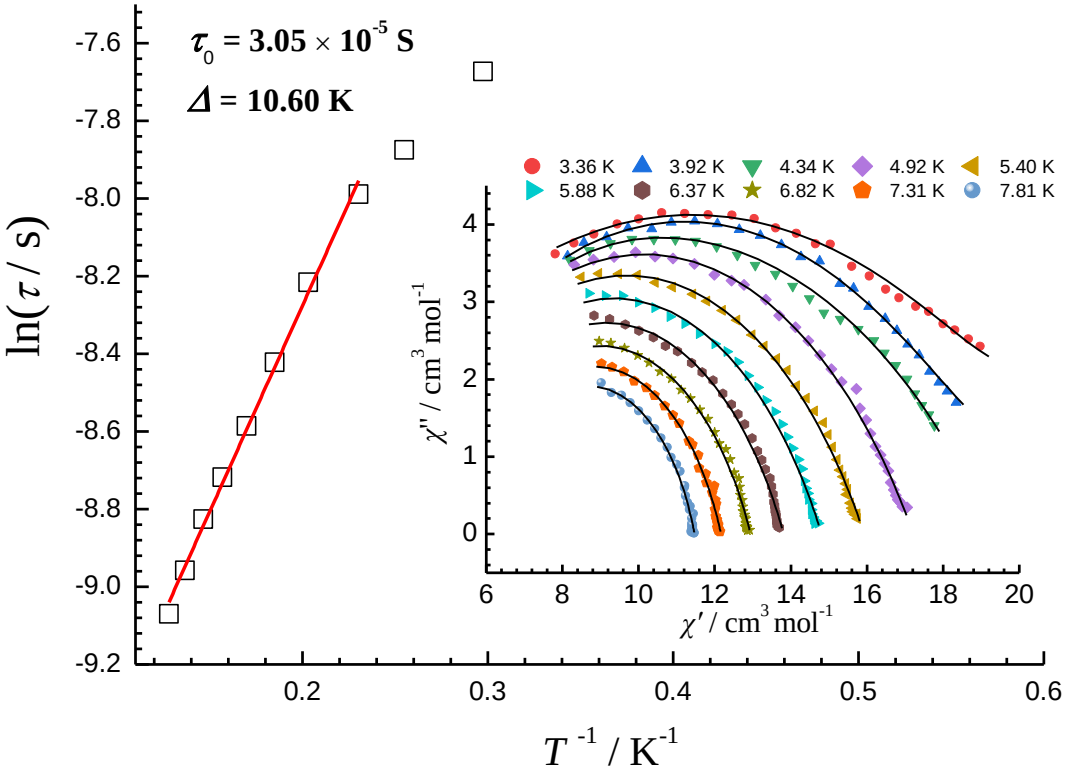

Figure S11. Variable-frequency ac magnetic susceptibility signals for **2Dy** under 2500 Oe dc field from 3.36 to 7.81 K (a); Plots of ln(τ) versus 1/T for **2Dy** and the linear fitting (b); Inset: Cole–Cole plots for **2Dy** obtained under 2500 Oe dc field.

(a)

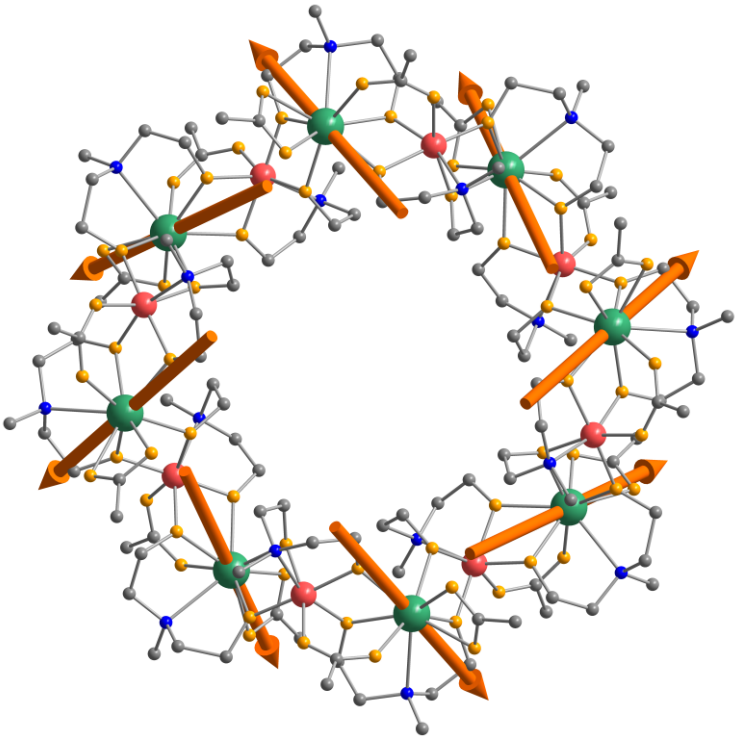

(b)

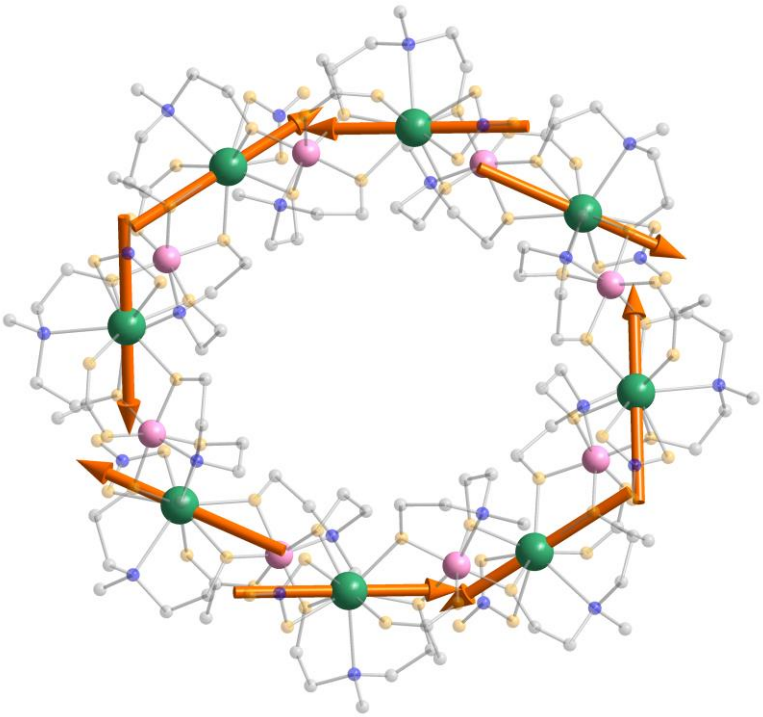

Figure S12. The ground state anisotropy directions (orange arrows) for the Dy^{III} ions in **1Dy** (a) and **2Dy** (b).

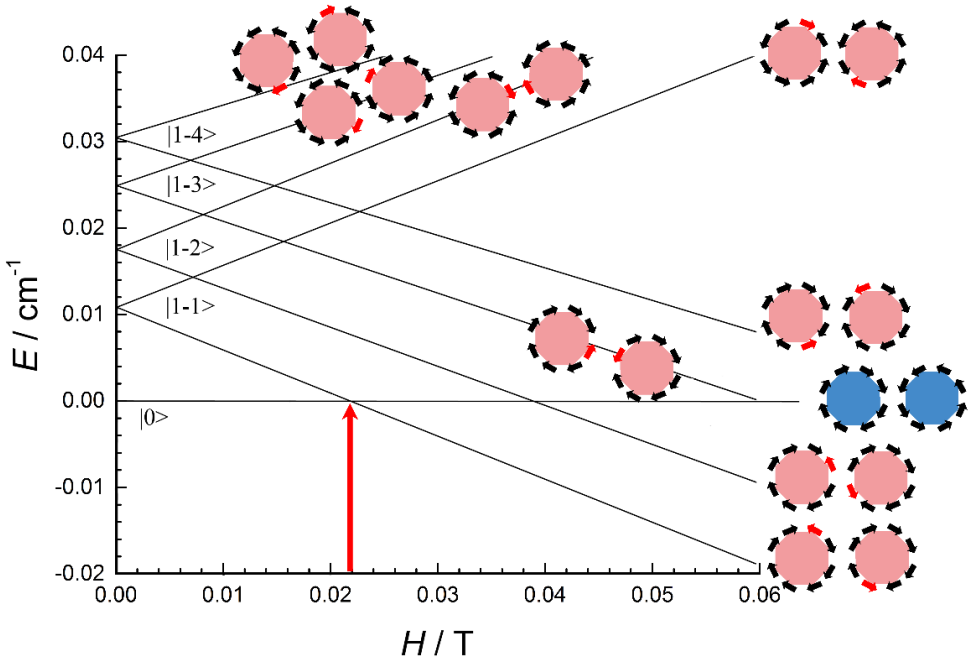

Figure S13. Energy levels for **2Dy** as function of magnetic field (Zeeman spectrum). Schematic non-collinear magnetic structure of the ground state (blue) and the first excited state (pink) of **2Dy**. Red vertical arrow represents the level crossing point at 0.022 T. The short arrows surrounding the circle are the local magnetic moments of Dy^{III} in the ground exchange doublet, in which red arrows represent the reversal of magnetization directions while the black ones represent original magnetization directions.

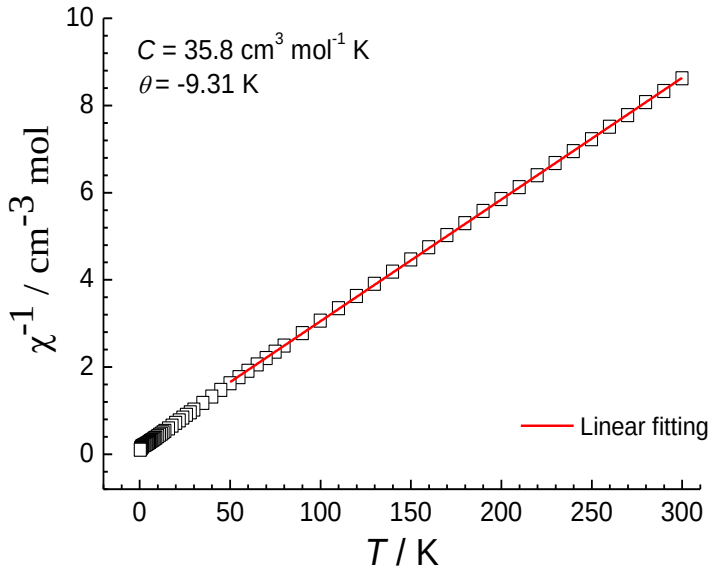

Figure S14. The Curie-Weiss fittings of the χ^{-1} vs. T plot under 1000 Oe dc field from 50 to 300 K for **1Y.**

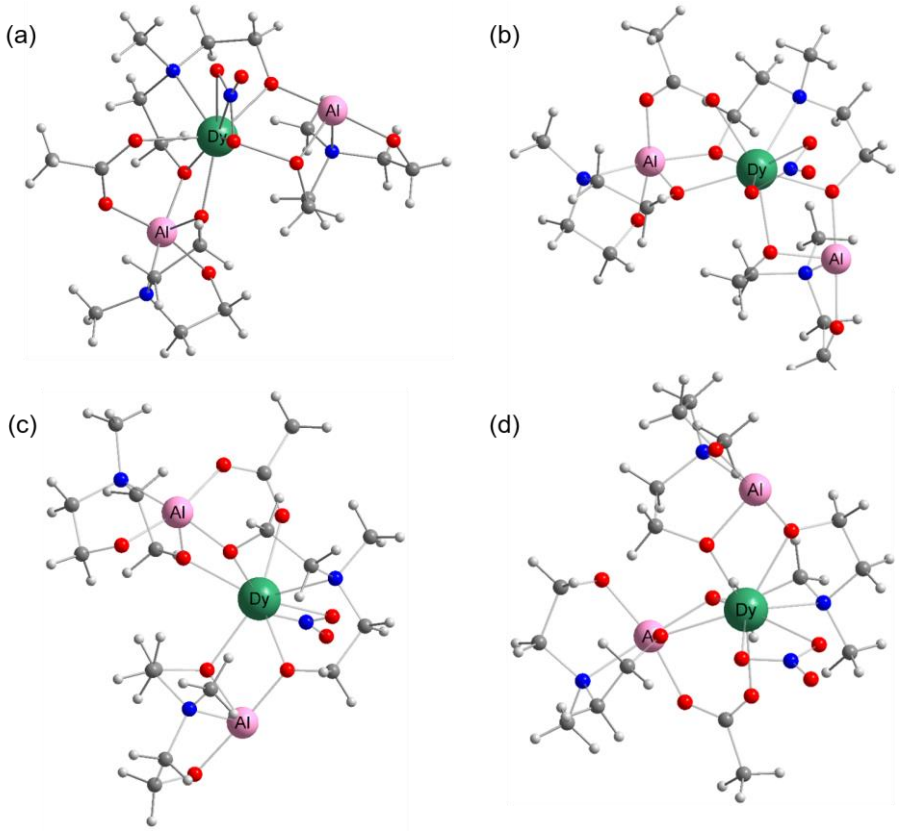

Figure S15. Calculated structure of the **2Dy-1** (a), **2Dy-2** (b), **2Dy-3** (c), and **2Dy-4** (d) fragment.

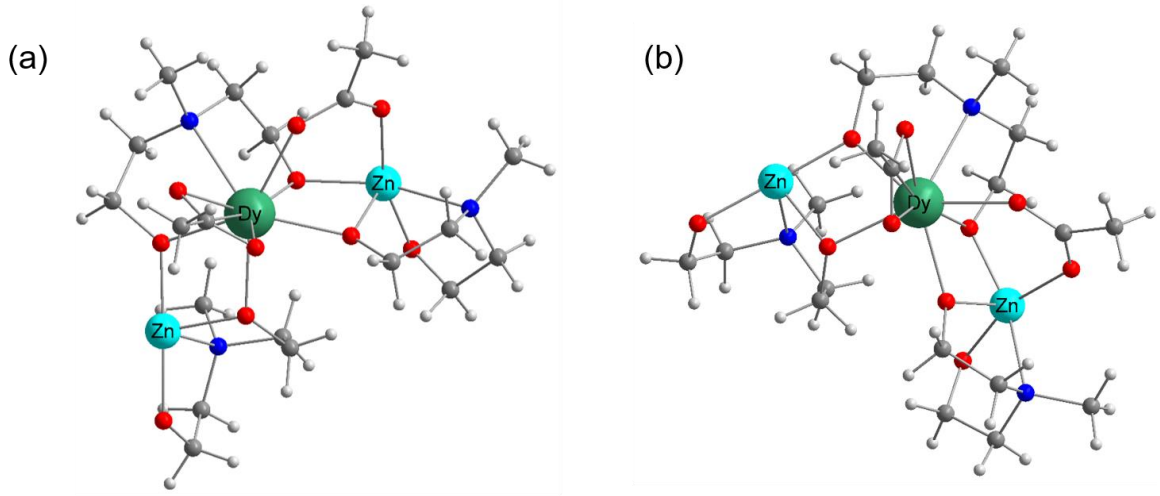

Figure S16. Calculated structure of the **1Dy-1** (a), **1Dy-2** (b) fragment.

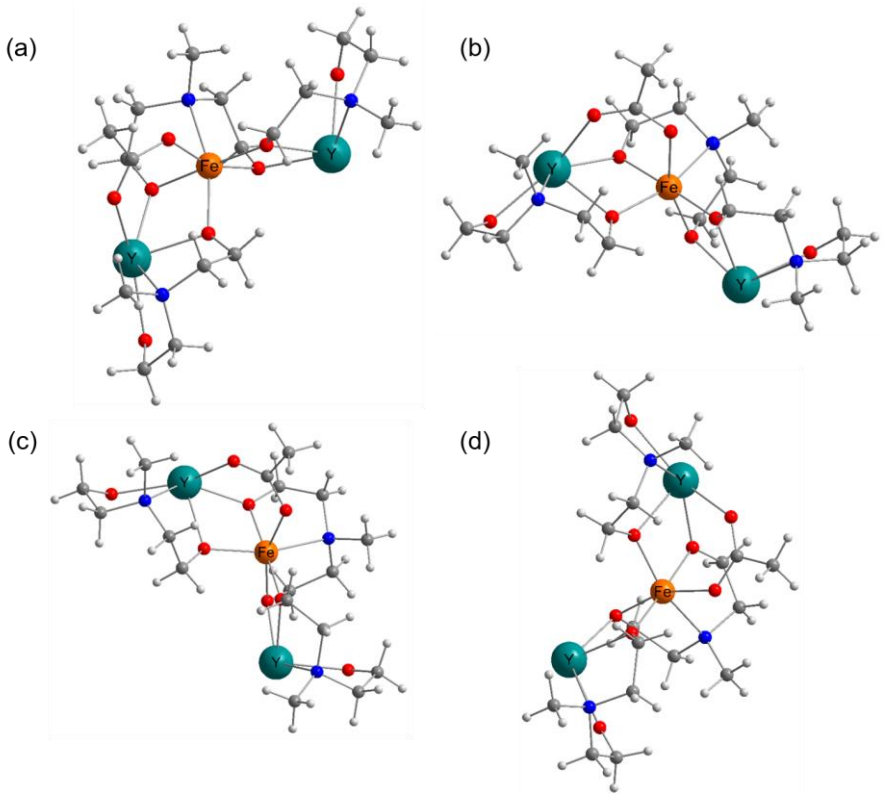

Figure S17. Calculated structure of the Fe1 (a), Fe2 (b), Fe3 (c), and Fe4 (d) fragment in **1Y.**

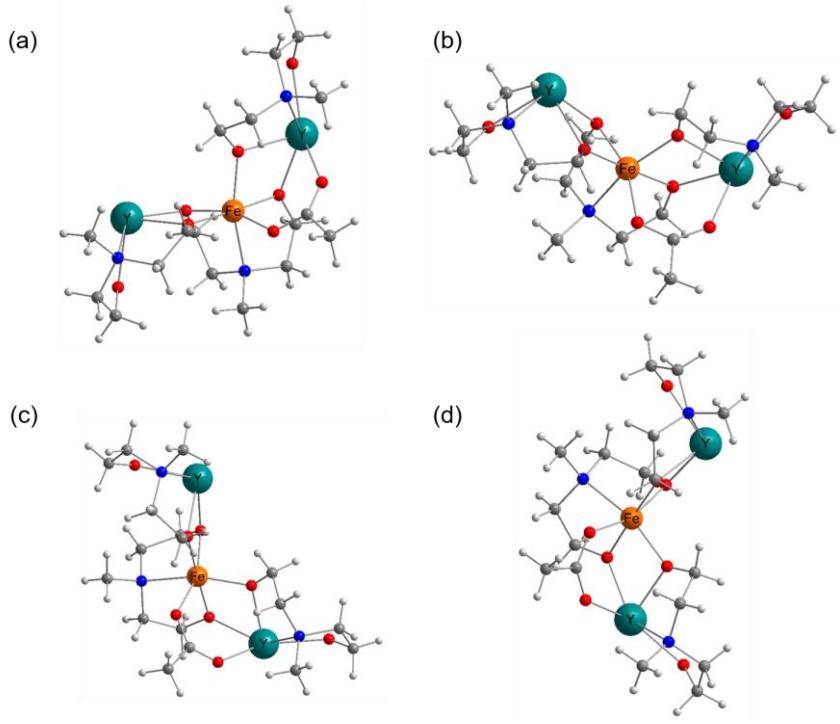

Figure S18. Calculated structure of the Fe5 (a), Fe6 (b), Fe7 (c), and Fe8 (d) fragment in **1Y.**

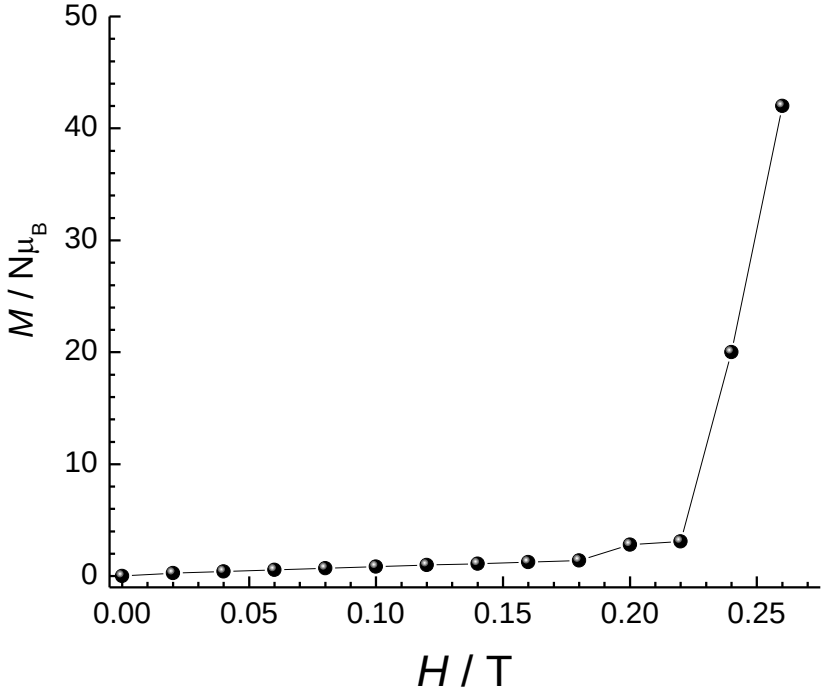

Figure S19. The simulations of field-dependent magnetization plots of **2Dy** at T ≈ 0 K.

II. Supplemental Tables

Table S1. Crystal data and structure refinement for **1Dy, 1Y** and **2Dy**.

	1Dy	**1Y**	**2Dy**
Compound	Fe_8Dy_8	Fe_8Y_8	Al_8Dy_8
Formula	$C_{114}H_{263}N_{17}Fe_8Dy_8O_{82}$	$C_{122}H_{303}N_{21}Fe_8Y_8O_{96}$	$C_{100}H_{224}N_{26}Al_8Dy_8O_{81}$
*F*w (g mol^{-1})	4931.13	4758.80	4602.82
T (K)	100(2)	100(2)	150(2)
Wavelength (Å)	0.71073	0.71073	0.71073
Crystal system	Cubic	Cubic	Orthorhombic
Space group	*Pn-3n*	*Pn-3n*	*Fddd*
a (Å)	39.853(18)	39.865(2)	20.291(11)
b (Å)	39.853(18)	39.865(2)	47.280(3)
c (Å)	39.853(18)	39.865(2)	76.050(4)
α (deg.)	90	90	90
β (deg.)	90	90	90
γ (deg.)	90	90	90
V (Å^3)	63300(5)	63358(5)	72960(70)
Z	12	12	16
D (g cm^{-3})	1.552	1.497	1.617
μ (mm^{-1})	3.405	2.793	3.359
F(000)	29496	29640	35136
Data / restraints / parameters	9322 / 26 / 476	9321 / 11 / 476	16075 / 0 / 977
Goodness-of-fit on F^2	1.175	1.092	1.177
R_1[a]	0.0874	0.1326	0.0516
wR_2 [b]	0.1896	0.2946	0.1391
CCDC Number	1942406	1942407	1942408

[a] $R_1 = \Sigma||F_o| - |F_c||/\Sigma|F_o|$, [b] $wR_2 = [\Sigma w(F_o^2-F_c^2)^2/\Sigma w(F_o^2)^2]^{1/2}$

Table S2. Selected bond lengths [Å] for **1Dy**.

Dy(1)-O(4)	2.298(8)	Dy(2)-O(14)	2.446(10)
Dy(1)-O(9)	2.310(9)	Dy(2)-N(4)	2.671(11)
Dy(1)-O(2)	2.322(8)	Fe(1)-O(3)	1.955(8)
Dy(1)-O(3)	2.331(8)	Fe(1)-O(12)#2	1.982(8)
Dy(1)-O(7)	2.395(8)	Fe(1)-O(2)	1.985(8)
Dy(1)-O(6)	2.418(9)	Fe(1)-O(1)	1.998(8)
Dy(1)-O(5)	2.433(9)	Fe(1)-O(16)#2	2.042(9)
Dy(1)-N(2)	2.661(10)	Fe(1)-N(1)	2.271(11)
Dy(2)-O(1)#1	2.298(8)	Fe(2)-O(11)	1.957(8)
Dy(2)-O(12)	2.312(8)	Fe(2)-O(10)	1.981(9)
Dy(2)-O(11)	2.318(8)	Fe(2)-O(9)	1.985(9)
Dy(2)-O(10)	2.328(8)	Fe(2)-O(4)	1.985(8)
Dy(2)-O(15)	2.381(8)	Fe(2)-O(8)	2.055(9)
Dy(2)-O(13)	2.427(8)	Fe(2)-N(3)	2.301(12)

Symmetry transformations used to generate equivalent atoms: #1 x,-z+1/2,y#2 x,z,-y+1/2

Table S3. Selected bond lengths [Å] for **2Dy**.

Al(1)-N(3)	2.127(10)	Al(4)-O(33)	1.883(8)	Dy(3)-N(7)	2.571(9)
Al(1)-O(2)	1.861(8)	Al(4)-O(34)	1.885(8)	Dy(3)-N(9)	2.878(9)
Al(1)-O(6)	1.887(7)	Al(4)-O(35)	1.908(8)	Dy(3)-O(16)	2.292(7)
Al(1)-O(7)	1.885(8)	Dy(1)-N(1)	2.596(9)	Dy(3)-O(18)	2.369(7)
Al(1)-O(8)	1.915(8)	Dy(1)-N(2)	2.862(9)	Dy(3)-O(19)	2.479(8)
Al(1)-O(13)	1.874(8)	Dy(1)-O(1)	2.296(7)	Dy(3)-O(21)	2.450(7)
Al(2)-N(5)	2.139(10)	Dy(1)-O(2)	2.328(7)	Dy(3)-O(22)	2.301(7)
Al(2)-O(14)	1.848(7)	Dy(1)-O(3)	2.435(7)	Dy(3)-O(23)	2.317(7)
Al(2)-O(15)	1.880(8)	Dy(1)-O(5)	2.472(8)	Dy(3)-O(24)	2.330(7)
Al(2)-O(16)	1.898(7)	Dy(1)-O(6)	2.320(7)	Dy(4)-N(10)	2.592(8)
Al(2)-O(17)	1.905(8)	Dy(1)-O(34)#1	2.279(7)	Dy(4)-N(11)	2.880(9)
Al(2)-O(22)	1.866(7)	Dy(1)-O(36)#1	2.371(7)	Dy(4)-O(25)	2.323(7)
Al(3)-N(8)	2.149(10)	Dy(2)-N(4)	2.591(9)	Dy(4)-O(27)	2.369(7)
Al(3)-O(23)	1.855(8)	Dy(2)-N(6)	2.865(10)	Dy(4)-O(28)	2.281(7)
Al(3)-O(24)	1.881(7)	Dy(2)-O(7)	2.293(7)	Dy(4)-O(29)	2.315(7)
Al(3)-O(25)	1.871(7)	Dy(2)-O(9)	2.357(7)	Dy(4)-O(30)	2.483(8)
Al(3)-O(26)	1.906(8)	Dy(2)-O(10)	2.435(7)	Dy(4)-O(32)	2.463(7)
Al(3)-O(28)	1.862(7)	Dy(2)-O(12)	2.481(8)	Dy(4)-O(33)	2.322(7)
Al(4)-N(12)	2.142(9)	Dy(2)-O(13)	2.299(7)	O(1)-Al(4)#1	1.868(7)
Al(4)-O(1)#1	1.868(7)	Dy(2)-O(14)	2.327(7)	O(34)-Dy(1)#1	2.279(7)
Al(4)-O(29)	1.851(8)	Dy(2)-O(15)	2.323(7)	O(36)-Dy(1)#1	2.371(7)

Symmetry transformations used to generate equivalent atoms: #1 x,-y+3/4,-z+3/4

Table S4. The *CSM* values calculated by *SHAPE* 2.1 for **1Dy** and **2Dy**.

Coordination Geometry	Atom	**1Dy**	**2Dy**
Octagon (D_{8h})		44.987	44.380
Heptagonal pyramid (C_{7v})		33.028	35.881
Hexagonal bipyramid (D_{6h})		31.189	32.254
Cube (O_h)		32.945	32.239
Square antiprism (D_{4d})		26.172	27.029
Triangular dodecahedron (D_{2d})		25.059	25.688
Johnson gyrobifastigium J26 (D_{2d})	Dy	29.763	26.693
Johnson elongated triangular bipyramid J14 (D_{3h})		41.166	39.180
Biaugmented trigonal prism J50 (C_{2v})		22.921	25.514
Biaugmented trigonal prism (C_{2v})		24.227	25.530
Snub diphenoid J84 (D_{2d})		23.246	26.450
Triakis tetrahedron (T_d)		31.386	31.536
Elongated trigonal bipyramid (D_{3h})		37.867	36.399

Table S5. The fit parameters of Cole-Cole plots for **2Dy**.

T / K	τ / s	α
3.36	4.65357×10^{-4}	0.51822
3.92	3.80131×10^{-4}	0.42390
4.34	1.73191×10^{-4}	0.06182
4.92	2.70238×10^{-4}	0.39790
5.40	2.19890×10^{-4}	0.37412
5.88	1.86709×10^{-4}	0.34987
6.37	1.63560×10^{-4}	0.32387
6.82	1.46811×10^{-4}	0.29338
7.31	1.28718×10^{-4}	0.26160
7.81	1.15114×10^{-4}	0.22864

Table S6. SA-CASSCF/RASSI calculated electronic states for **2Dy-1**.

Energy (cm^{-1})	g_x	g_y	g_z	Wavefunction
0	0.00	0.01	19.86	99.1%|±15/2>
176	0.10	0.13	16.88	94.2%|±13/2>
231	2.2	5.8	10.57	61%|±11/2> + 23%|±3/2>
288	8.6	7.2	0.50	13%|±11/2> + 17%|±1/2> + 39%|∓1/2> + 11%|∓9/2>
313	0.7	2.8	11.98	22%|±9/2> + 17%|±5/2> + 37%|∓3/2>
364	0.3	1.7	13.73	21%|±9/2> + 24%|±5/2> + 29%|∓7/2>
408	1.4	2.0	14.40	23%|±9/2> + 14%|±5/2> + 21%|±1/2> + 12%|∓3/2> + 29%|∓7/2>
436	1.3	2.5	16.49	35%|±7/2> + 21%|±3/2> + 31%|∓5/2>

[a] Only components with > 10% contribution are given, rounded to the nearest percent.

Table S7. SA-CASSCF/RASSI calculated electronic states for **2Dy-2**.

Energy (cm^{-1})	g_x	g_y	g_z	Wavefunction
0	0.00	0.01	19.46	97.1%|±15/2>
154	0.13	0.21	16.21	91.2%|±13/2>
212	1.7	7.3	9.64	43%|±11/2> + 21%|±3/2> + 10%|∓1/2>
259	7.3	6.8	3.40	11%|±9/2> + 37%|±1/2> + 24%|∓1/2>
298	1.9	3.7	10.03	12%|±9/2> + 28%|±5/2> + 32%|∓3/2>
334	0.1	0.3	16.37	49%|±9/2> + 10%|±5/2> + 34%|∓7/2>
365	3.7	5.4	13.74	20%|±11/2> + 11%|±5/2> + 21%|∓3/2> + 24%|∓7/2>
374	1.7	2.9	17.49	54%|±7/2> + 23%|±3/2> + 27%|∓5/2>

[a] Only components with > 10% contribution are given, rounded to the nearest percent.

Table S8. SA-CASSCF/RASSI calculated electronic states for **2Dy-3**.

Energy (cm^{-1})	g_x	g_y	g_z	Wavefunction
0	0.00	0.00	19.88	99.2%|±15/2>
191	0.10	0.12	16.88	94.1%|±13/2>
257	1.4	3.7	12.32	79%|±11/2> + 10%|±3/2>
307	9.3	5.9	0.24	13%|±9/2> + 17%|±1/2> + 32%|∓1/2>
347	1.4	3.7	13.13	34%|±9/2> + 27%|±7/2> + 21%|∓1/2>
378	2.5	3.7	10.13	31%|±9/2> + 24%|±5/2> + 19%|∓5/2>
418	2.7	3.4	12.43	26%|±7/2> + 10%|±5/2> + 10%|±1/2> + 13%|∓3/2>
421	3.7	5.6	11.49	31%|±7/2> + 16%|±3/2> + 29%|∓5/2>

[a] Only components with > 10% contribution are given, rounded to the nearest percent.

Table S9. SA-CASSCF/RASSI calculated electronic states for **2Dy-4**.

Energy (cm^{-1})	g_x	g_y	g_z	Wavefunction
0	0.00	0.01	19.87	99.2%|±15/2>
167	0.10	0.13	16.86	94.3%|±13/2>
224	2.7	5.9	11.03	62%|±11/2> + 24%|±3/2>
279	5.6	4.2	3.05	11%|±11/2> + 37%|±1/2> + 14%|∓7/2>
301	0.7	6.3	10.58	25%|±9/2> + 49%|∓3/2>
347	1.2	3.8	14.39	22%|±9/2> + 29%|±5/2> + 31%|∓7/2>
389	2.4	4.0	16.41	21%|±7/2> + 14%|±3/2> + 10%|∓3/2> + 19%|∓5/2>
403	2.9	5.5	13.27	31%|±7/2> + 21%|±3/2>

[a] Only components with > 10% contribution are given, rounded to the nearest percent.

Table S10. The individual deviation angles from the plane and corresponding Ising interactions of **2Dy**. (in cm^{-1})

	$cos\varphi$	$\widetilde{J_\iota}$
2Dy-1 with 2Dy-2	-0.10009	0.02502
2Dy-2 with 2Dy-3	-0.06993	0.01748
2Dy-3 with 2Dy-4	-0.12242	0.0306
2Dy-4 with 2Dy-1'	-0.04336	0.01084
…		

Table S11. The angle (θ) of anisotropy axis tilting with Dy_8 plane in **2Dy**.

Anisotropy axis	θ / ∘
2Dy-1	44.55
2Dy-2	42.01
2Dy-3	42.64
2Dy-4	42.01
2Dy-1'	44.55
2Dy-2'	42.01
2Dy-3'	42.64
2Dy-4'	42.01

Table S12. The calculated *g* tensors for the lowest and four different kinds of first excited Kramers doublets of **2Dy**.

	|0>	|1-1>	|1-2>	|1-3>	|1-4>
g_y	0.00	0.00	0.01	0.01	0.03
g_z	0.00	0.01	0.01	0.04	0.07
g_x	0.42	39.37	38.14	38.32	37.10

Table S13. The magnetic parameters of **1Y** extracted from *ab initio* calculations.

	D (cm^{-1})	E/D	g_x	g_y	g_z
Fe1	-0.32	0.20	1.99	1.99	1.99
Fe2	-0.14	0.20	1.99	1.99	1.99
Fe3	-0.31	0.21	1.99	1.99	1.99
Fe4	-0.17	0.20	1.99	1.99	1.99
Fe5	-0.29	0.21	1.99	1.99	1.99
Fe6	-0.15	0.21	1.99	1.99	1.99
Fe7	-0.31	0.17	1.99	1.99	1.99
Fe8	-0.14	0.20	1.99	1.99	1.99

Table S14. SA-CASSCF/RASSI calculated electronic states for **1Dy-1**.

Energy (cm^{-1})	g_x	g_y	g_z	Wavefunction
0	0.43	1.21	18.16	70%|±15/2> + 23%|±13/2>
81	3.41	4.27	10.94	54%|±13/2> + 10%|±11/2> + 24%|±1/2>
154	0.9	4.9	9.87	41%|±11/2> + 13%|±9/2> + 25%|∓3/2>
203	8.1	5.1	4.21	10%|±13/2> + 12%|±11/2> + 58%|∓5/2>
231	1.2	3.4	13.73	12%|±15/2> + 21%|±7/2> + 57%|∓3/2>
304	3.1	4.5	8.67	31%|±9/2> + 24%|±7/2> + 17%|∓5/2>
378	0.9	1.2	16.32	25%|±13/2> + 10%|±3/2> + 23%|±1/2> + 29%|∓7/2>
405	1.7	3.4	13.27	35%|±7/2> + 31%|±3/2> + 10%|∓5/2> + 11%|±1/2> + 10%|∓7/2>

[a] Only components with > 10% contribution are given, rounded to the nearest percent.

Table S15. SA-CASSCF/RASSI calculated electronic states for **1Dy-2**.

Energy (cm^{-1})	g_x	g_y	g_z	Wavefunction
0	0.58	1.71	17.69	67%|±15/2> + 19%|±13/2> + 10%|±1/2>
62	2.74	3.98	12.74	63%|±13/2> + 34%|±1/2>
117	0.5	2.9	14.35	61%|±11/2> + 23%|±7/2> + 10%|∓3/2>
145	8.4	4.3	2.92	50%|±9/2> + 32%|±7/2>
169	0.3	1.9	16.14	14%|±15/2> + 41%|±9/2> + 17%|∓1/2>
214	4.3	6.9	7.84	34%|±7/2> + 37%|∓5/2>
269	3.1	4.9	11.12	40%|±3/2> + 13%|±1/2> + 19%|∓7/2>
324	1.2	2.7	15.41	29%|±3/2> + 37%|∓5/2> + 23%|±1/2> + 10%|∓11/2>

[a] Only components with > 10% contribution are given, rounded to the nearest percent.